Inelastic helium scattering studies of ordered Ar, Kr, and Xe monolayers physisorbed on Ag(111): Dispersion curves, scattering cross sections, and excitation line shapes

K. D. Gibson and S. J. Sibener[a)]
Department of Chemistry and The James Franck Institute, The University of Chicago, Chicago, Illinois 60637

(Received 16 September 1987; accepted 7 December 1987)

This paper is the first in a series covering our experiments examining the physical properties of ordered overlayers of Ar, Kr, and Xe physisorbed on Ag(111). In this paper, we examine the desorption kinetics of the Xe monolayer/Ag(111) system. Desorption is zeroth order until ~90% of the monolayer has desorbed, then becomes first order. We also measured the inelastic scattering of an 18 meV He beam from unconstrained monolayers of (111) oriented Ar, Kr, and Xe. The transitions are mapped across the entire surface Brillouin zone from $\bar{\Gamma}$ to $\bar{M}$. The data are dispersionless, indicating that for the measured mode the adatoms are behaving as independent Einstein oscillators. Parametrized physisorption potentials for RG–Ag(111) [RG = Ar, Kr, Xe] are constructed using these results. Inelastic scattering probabilities and linewidths are also presented. The inelastic scattering probabilities vary by at most a factor of 3 across the entire surface Brillouin zone, and are reported as a function of incident angle, final wave vector, and surface temperature. Variations in the inelastic scattering probabilities are indicative of dynamical adatom–substrate coupling. Experimental techniques which turn these dynamical couplings on or off for the same phonon energy are discussed. Limited results for clean Ag(111) are also presented. It is hoped that these measurements, on such ideal systems as ordered rare gas monolayers, will provide further impetus for developing improved theoretical treatments of inelastic single phonon scattering.

INTRODUCTION

The physisorption of rare gases has been a field of continuing interest. A brief review of some of the work done on rare gas monolayers is given by Birgenau and Horn.[1] The properties of rare gas solids have been extensively studied,[2] and because of this and the relative simplicity of their interactions, they serve as excellent model systems for our understanding of adsorption phenomena. Much of the previous work has involved physisorption on exfoliated graphite. This is because of the poor surface sensitivity of the probes used, requiring the substrate to have a large specific surface area. With surface sensitive probes, it is possible to study physisorption on a wider range of substrates.

There has also been some work on single metal crystals, some of the most extensive being from the studies of Webb, Bruch *et al.* for the physisorption of Ar, Kr, and Xe on the (111) face of Ag.[3–9] The experimental technique used in these studies was low energy electron diffraction (LEED), and they were able to measure the thermodynamic and structural properties of constrained and unconstrained monolayers with a high degree of accuracy. One feature of using Ag(111) is that, unlike graphite, all of the rare gas monolayers are azimuthally aligned but translationally incommensurate with the substrate at most coverages and surface temperatures where ordered islands are present. Their results seem to indicate that the substrate can be treated, to a very good first approximation, as a smooth dielectric continuum. The fact that there is no site specificity for rare gas adsorption implies that, to a good approximation, that the Ag substrate simply provides a uniform holding potential, and the surface structure of the monolayers is determined by the lateral interactions of the adatoms.

In light of the available information for these systems, we undertook a series of experiments to investigate the elastic and inelastic scattering of a He atomic beam, a highly surface sensitive technique, from unconstrained rare gas monolayers physisorbed on Ag(111). These are attractive model systems for He scattering because the gas phase He–rare gas and rare gas–rare gas pair potentials are well known. This provides a good test of using sums of pair potentials to theoretically model the scattering results, and allows a more accurate assessment of the role of multibody interactions. Also, since the monolayer structures are not dependent on the substrate structure, the effect of the Ag on the He scattering can be treated with a simple long range van der Waals attraction. Vibrational spectroscopy, done at discrete positions across the surface Brillouin zone (SBZ), allows us to have a microscopic look at the adsorbed rare gas–rare gas and rare gas–substrate interactions. This is a useful adjunct to the average thermodynamic properties from the LEED experiments.

This paper deals primarily with the inelastic scattering of He from the rare gas monolayers. Preliminary results have already been reported.[10–12] This is the first in a series of papers that will discuss our results for elastic and inelastic He scattering from monolayer to many layers. Inelastic scattering experiments on monolayers of rare gases have been done in the past. Taub *et al.*[13] used neutron scattering to examine Ar^{36} adsorbed on exfoliated graphite. Neutron scattering is not a surface sensitive probe, however, and of the rare gases,

[a)] Alfred P. Sloan Fellow, 1984–1987.

 0021-9606/88/127862-31$02.10

only Ar^{36} has a reasonably large scattering cross section for neutrons. Mason and Williams[14–16] have also examined the inelastic scattering of He from rare gases physisorbed on other single crystal metal surfaces. However, our studies are the first to examine both the elastic and inelastic scattering of He from a series of rare gas overlayers on a layer-by-layer basis, from monolayer to many layers. Subsequent inelastic scattering measurements of Xe physisorbed on Pt(111) by Kern *et al.*[17] have revealed similar behavior as that reported here.

There are at least three requirements for doing high resolution surface vibrational spectroscopy on these physisorbed monolayers. These are (1) high surface sensitivity, (2) sufficient momentum to probe the entire SBZ, and (3) high energy resolution, since the transition energies observed are, in general, only a few meV. (An energy resolution of $\leqslant 0.5$ meV was routinely achieved in our experiments.) A comparison of the various spectroscopies is given in Ref. 18. Only He scattering meets all three requirements. Electron energy loss spectroscopy (EELS) might be a close second but at the present time, a 5 meV energy resolution is considered quite good, and this is not small enough to resolve the observed transitions and line shapes.

The procedure used was to measure the angle resolved time of flight of the inelastically scattered He. The short flight path of our machine largely dictated the use of an 18 meV He beam. A higher energy beam would have made it difficult to resolve the low energy transitions observed for scattering from these surfaces. Since we are primarily interested in interactions with single phonons, and the monolayers are very "soft" surfaces, a low energy beam is preferred for oberving these single phonon events.[19] Also, since the energies of the transitions are only on the order of a few meV, we do not have to contend with the "slow collision effect",[20] the condition that $\nu_{\text{phonon}} < v_{\text{beam}}/\Lambda$ (Λ is the interaction length of the He $\{\sim 1$ Å$\}$ and v_{beam} is the beam velocity), which makes it difficult to observe high energy modes with a low energy beam. The phonon modes can then be mapped as a function of momentum transfer across the entire SBZ by varying the final scattering angle that was probed. It is important to note that we mapped the phonons by varying just the detector angle, keeping the incident angle fixed. Though this does not totally eliminate the effects of selective adsorption resonances on the inelastic scattering probabilities, an important contribution for highly corrugated surfaces, it reduces the number of ways that they can influence the relative probabilities across the SBZ.

The first section of this paper outlines the experimental techniques. We then report some experiments that examined the desorption and adsorption of Xe, including the desorption kinetics of the monolayer. The next section deals with the inelastic scattering of He from Ar, Kr, and Xe monolayers along the $\langle 11\bar{2}\rangle$ azimuth. For all of the monolayers, the observed phonon mode is dispersionless, indicating that the adatoms are behaving as independent Einstein oscillators, vibrating in the rare gas–Ag holding potential. The vibrational modes of the surface have been quantitatively modeled, assuming a rigid substrate, and the results presented elsewhere.[21,22]

We also examine the inelastic scattering probabilities and linewidths. The inelastic scattering probabilities are highly dependent on the nature of the He–surface interaction potential, but there is also a possibility that they might show vibrational coupling between the overlayer and the substrate,[23] and these rare gas monolayer systems allow an interesting test of this theory. The frequency of the Einstein oscillator mode overlaps the frequency of the surface projection of the bulk Ag modes near $\bar{\Gamma}$ (the center of the first SBZ), and crosses that of the sagittally polarized (polarized in the scattering plane) Rayleigh wave about midway across the SBZ. Near $\bar{M}$ (the edge of the first SBZ), the frequency of the Einstein mode lies well below any of the surface modes of the Ag. Our results show evidence that, at the position in reciprocal space where the energy of the monolayer Einstein mode is coincident with the Ag Rayleigh mode, there is an enhancement in the inelastic scattering probabilities, which could be due to a resonance between the adatom vibrations and the substrate surface mode. The linewidths of the inelastic scattering are broader near $\bar{\Gamma}$ than $\bar{M}$. This observation could be due to mixing of the Einstein mode with the surface projection of the substrate vibrational modes. At $\bar{M}$, the only way for energy to decay into the Ag substrate is through anharmonic coupling terms. These observations demonstrate the utility of inelastic He scattering to examine dynamical effects of the substrate on the dynamics of the overlayer. A preliminary report discussing these effects was previously presented.[12]

EXPERIMENTAL

The He used was Air Products Zero Grade (99.995%), which was further purified during use by passing it through a liquid nitrogen cooled coil of tubing containing a molecular sieve (Linde type 13X-PLTS, 1/16 in.). The principle contaminant after this procedure was Ne, which presented no problem at the temperature of the experiments.

A supersonic expansion from a liquid nitrogen cooled source, which we designed and built, produced the He molecular beam. Precooling of the room temperature He was accomplished by having the gas pass through a coil of stainless steel tubing contained within a larger stainless steel can. The can was filled with the liquid cryogen from the bottom by the slight pressurization of an external 50 ℓ Dewar. On the top of the can is the exhaust vent. By maintaining a slight overpressure in the Dewar, a slow drip of liquid nitrogen from the exhaust was maintained, insuring that the can was always filled. Immediately after passing through the can, the tubing containing the He was welded to a Cajon VCO fitting, modified so that it held the nozzle, a Ni pinhole from Ealing Optical. This design allows for the easy replacement of nozzles if one becomes clogged, or a different size pinhole is desired. On the nozzle side of the can, a copper plate is screwed on, with an indium gasket maintaining good thermal contact. To this are braized two large copper braids. The other end of these braids are braized to two copper blocks which were machined to fit around the VCO fitting. By bolting these two blocks onto an indium gasket near the end of the fitting, nearly liquid nitrogen temperatures were main-

tained at the nozzle. The can was insulated with aluminized Mylar, and sat in the source chamber vacuum, with the cryogen connections made to the outside through 3/8 in. SS bellows and a Huntington Vacuum feedthrough. As long as there was some liquid nitrogen coming from the exhaust, the beam temperature stability was better than ± 1 K during the course of several hours running. For these experiments, the He beam was expanded through a 12 μ pinhole at a stagnation pressure of 600 psi. The beam energy was typically 18 meV, with a $\Delta v/v \approx 1.2\%$.

The source chamber was pumped by a VHS-6 diffusion pump which was bolted directly to the bottom of the chamber, and a VHS-4 diffusion pump which was connected to the side through a copper elbow and a 4 in. gate valve. The pressure in this region with the beam on was in the mid-10^{-4} Torr range. Before entering the next stage of differential pumping, the beam was skimmed with a Beam Dynamics skimmer (model UC-1, 0.0223 in. aperture). The third differential pumping region contained a shutter and the chopper. This was a dynamically balanced aluminum disk with eight 0.020 in. slots on a working diameter of 5.75 in. This disk was spun by a TRW AC hysteresis motor, the rate being precisely controlled with a variable frequency sine wave generator and an audio amplifier. For most of the experiments reported here, the frequency was 350 Hz. One side of the chopper disk was polished for high reflectivity. Light from a collimated penlight bulb reflecting off this surface was picked up by a silicon photodiode to use for synchronizing the chopper and the counting electronics.

The 0.020 in. collimating aperture for the beam separated this region from a small final differential pumping region, after which the beam enters the scattering chamber (base pressure 2×10^{-10} Torr), with an approximately 0.13° angular divergence. This chamber contained the crystal manipulator and detector on independently rotating feedthroughs, allowing the incident angle and scattering angle probed to be independently varied. This chamber was pumped by a 400 ℓ/s ion pump. The detector was an Extranuclear quadrupole mass spectrometer, using an electron impact ionizer with a very narrow ionization length parallel to the flight path. Transmitted ions are detected with a venetian blind electron multiplier, suitable for pulse counting. The detector was differentially pumped with two 60 ℓ/s ion pumps. Angular acceptance was 0.67°, chopper to crystal distance was 21.53 cm, and crystal to ionizer distance was 14.45 cm. Further details on the machine can be found in Ref. 24.

Time-of-flight (TOF) data collection was done with a multichannel scalar, interfaced to a PDP-11 minicomputer through a CAMAC system. For the phonon spectra, 1 μs channels were used, with 0.25 μs channels used for the straight-through beam, which was used to calibrate the incident beam conditions.

The substrate for these experiments was a single crystal of Ag from a 99.999% pure boule grown at the Cornell Material Preparation Laboratory, cut and polished within 0.5° of the (111) plane. Further treatment at our laboratory consisted of repolishing with fine cerium oxide powder, and chemical polishing with a saturated chromic acid-10% HCl solution, followed by a brief treatment with 10% HNO_3. The orientation was checked using Laue x-ray back reflection. The crystal was spotwelded to the platinum support rods of the crystal manipulator, and a chromel–alumel thermocouple was welded to the back.

The crystal manipulator was designed to give translational, tilt, and azimuthal adjustments. The platinum support rods for the crystal were welded to larger tungsten rods. These were electrically and thermally isolated from the rest of the manipulator by alumina spacers. Copper clamps welded to OFHC copper braids connected these rods to a floating power supply, so that the crystal could be resistively heated. Cooling was accomplished with an Air Products Heli-Tran transfer tube, which delivered liquid He to a cold tip inside the scattering chamber. Connection to the copper braids was done through thin slabs of sapphire cut along the C axis to provide good thermal conductivity to, and electrical insulation of, the crystal. The crystal temperature was controlled with a homemade circuit which regulated the current of the power supply, using feedback from the thermocouple. For low temperature runs, the temperature stability was best controlled ($\leqslant 1$ K) by adjusting the flow rate of the liquid He to the cold tip. The lowest temperature achievable was 20 K.

Once the sample was mounted in the scattering chamber, the thermocouple was calibrated. This was done three ways. First, before pumping down, thermocouple voltage readings were taken when the crystal was immersed in liquid nitrogen and a dry ice–acetone bath. After bakeout, the chamber was backfilled with Kr at different pressures, and the onset of monolayer adsorption as a function of temperature was observed, using He specular reflection. The temperature could then be calibrated against the phase diagram from Unguris *et al.*[8] The final way was to run trilayer Xe isothermal desorptions at different temperatures, and compare these results to those of trilayer Xe on W(110) (Opila *et al.*[25]), which should be similar. We think that the temperature calibration is good to within 3 K.

After system bakeout, the Ag sample was cleaned by argon ion bombardment. This consisted of mechanically rastering the sample across the ion beam (1 kV, 3 μA), while it was heated to 500 K. The crystal was then annealed at 750 K for approximately 30 min. Cleanliness was checked by Auger spectroscopy. For these experiments, the crystal had to be scrupulously clean. Small amounts of Cl ($\sim 1\%$ as determined by Auger spectroscopy) on the surface caused the rare gas monolayers to grow as islands of different azimuthal alignment, rotated by 30° with respect to one another. Coherence was checked by observing the He reflectivity ($\Theta_i = 50°$) at room temperature. Specular reflectivities were on the order of 10%. By comparing the width of the reflected beam to that of the straight-through beam, which has the width of the instrument function, simple perturbation theory[26] indicated that the coherence length was ~ 100 Å. Azimuthal alignment was checked by observing H_2 diffraction from the liquid nitrogen cooled crystal. The Auger spectrum and He reflectivity were routinely checked on days when experiments were run. If any problem was observed, the crystal was sputtered and annealed before proceeding.

Structural and thermodynamic information for these rare gas monolayers was already available from the work of

Unguris *et al.*[3,6,8] With the phase diagrams from these papers, we formulated a method for growing ordered and reproducible monolayers. Dosing was done with a low pressure side beam, inclined at 15° to the scattering plane. By means of a shutter, this beam could be flagged on and off within a few milliseconds before entering the scattering chamber. The pressure at the crystal surface due to the dosing beam was approximately 10^{-7} Torr, and the spot diameter was approximately 0.10 in., twice that of the He beam.

To grow the Xe monolayer, the crystal was dosed at $\Theta_i = 0°$ for 1 min, $T_s = 74$ K (for the growth conditions, all temperatures are approximate). Then, with the dosing beam still on, the temperature was dropped to 56 K. At this point, the dosing beam was stopped, and the crystal rotated to $\Theta_i = 70°$. The crystal was then dosed for another minute at 56 K. The temperature was then dropped to 24 K, then reheated to 56 K for at least 5 min to anneal the Xe overlayer. Kr monolayers were grown similarly, except that the first temperature was 52 K, and the temperature of the second dose and anneal was 41 K. Ar monolayers were grown by first dosing at 43 K for 1 min, $\Theta_i = 70°$. With the dosing beam still on, the temperature was dropped to 27 K. Just as this temperature was reached, the dosing beam was flagged off. The surface was allowed to anneal at this temperature for at least 10 min, or a partial bilayer still existed.

That there was at least full monolayer coverage could be confirmed by observing the specular He reflection from the surface. Since the clean Ag surface had a reflectivity of approximately 90% at low surface temperatures, as compared to about 1% for a rare gas monolayer, a small amount of uncovered Ag would result in a large specular signal. When we purposely dosed for only a few seconds, shorter than the time necessary for full monolayer coverage given the dosing beam pressure, the diffraction peaks were present, but the specular intensity would be close to that of clean Ag. That only a monolayer was present could be confirmed with temperature programmed thermal desorption (TPD), where the surface temperature was ramped at about 2 K/s, and the rare gas desorption was monitored with the mass spectrometer. Due to the influence of the rare gas–Ag holding potential, the first layer of rare gas desorbed at a much higher temperature than any other layers. The presence of one peak in a TPD spectrum confirmed that there was only a monolayer.

The quality of the monolayers was checked by comparing the ratios of the intensities of the specular to the incident He beam, and by the ratio of some of the diffraction peaks to the specular. The ratio of I_{00}/I_0 had, at most, a 20% variation on a daily basis. (I_{mn} is the intensity of the diffraction rod due to $\mathbf{G}_{m,n}$ and I_0 is the intensity of the incident beam.) In the case of Xe, where the experiments were done over the course of a year, the total variation in this ratio was almost a factor of 2. This will be discussed more thoroughly in the section on inelastic scattering probabilities. For the ratio of diffraction peaks to I_0, the variation was only about $\pm 20\%$ for all the data used.

Figure 1 shows He diffraction spectra for the Ar, Kr, and Xe monolayers, taken along the $\langle 11\bar{2}\rangle$ azimuth. These spectra were taken at $\Theta_i = 45°$ with an 18 meV He beam.

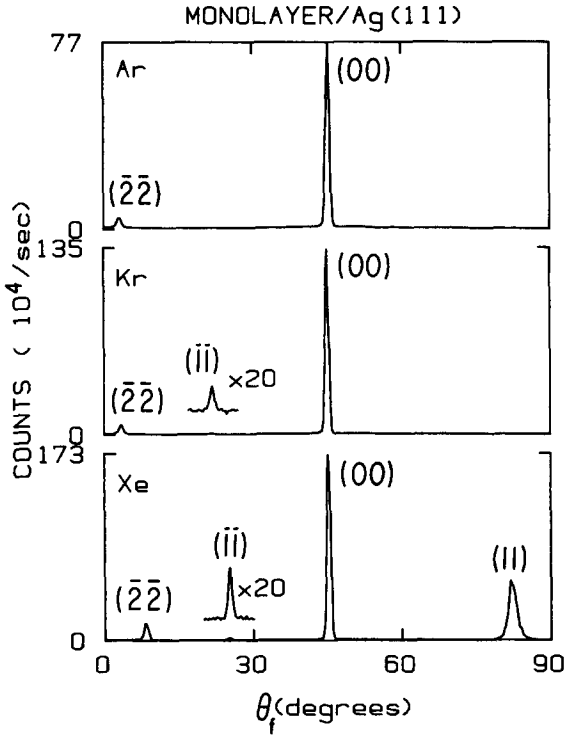

FIG. 1. Diffraction spectra for Ar, Kr, and Xe monolayers along the $\langle 11\bar{2}\rangle$ azimuth, taken at $\Theta_i = 45°$ with an 18 meV He beam. Surface temperatures were 22 K for Kr and Xe, and 21 K for Ar. The absolute intensities are only roughly comparable, as the experimental conditions were not exactly the same for all three spectra. All kinematically allowed elastic features are visible except for Ar, where the signal from the $(\bar{1}\bar{1})$ diffraction peak is not visible above the noise.

Most of the expected orders of diffraction are seen, the incoherent background between elastic features is small, and the elastic features have a small angular width. These three attributes attest to the high degree of order for the monolayers, and indicates that we were not growing roughened films. The widths of the elastic features can be used to estimate the coherence length of the surface; i.e., the size of ordered adsorbate islands. After deconvolution of the specular peaks for the instrument function, the coherence length was estimated to be approximately 100 Å, and only slightly smaller than the Ag substrate. The positions of the elastic features also gives the lattice constants a parallel to the surface; for Ar $a = 3.79 \pm 0.02$ Å at $T_s = 21$ K, and for Kr $a = 4.02 \pm 0.02$ Å at $T_s = 24$ K. The final value for a Xe monolayer was about 4.38 Å at $T_s = 24$ K. This is the lattice constant after the monolayer was about an hour old. Immediately after dosing, it was as much as 0.05 Å larger. This slow compression of unconstrained Xe monolayers was also observed by Unguris *et al.*[6] Even after several hours, the measured lattice constant was still, on the average, larger than the bulk rare gas lattice constant.[27] However, the value for our Xe monolayers is about 0.04 Å smaller than that quoted by Unguris *et al.*[6] for an unconstrained monolayer.

Table I presents the experimental elastic scattering probabilities for the in-plane diffraction peaks of Fig. 1. A more thorough discussion of elastic diffraction will be given in a subsequent paper.[28]

TABLE I. Elastic scattering probabilities (in percent) for the diffraction spectra shown in Fig. 1. First number is Debye–Waller corrected to 0 K (see the text), the number in parentheses is the value before Debye–Waller correction.

Adsorbate	(11)	(00)	$(\bar{1}\bar{1})$	$(\bar{2}\bar{2})$
Ar	···	2.29(1.12)	0.003(0.002)	0.169(0.072)
Kr	···	3.76(1.94)	0.034(0.016)	0.270(0.120)
Xe	1.44(1.02)	2.52(1.59)	0.035(0.021)	0.278(0.156)

Xe MONOLAYER DESORPTION

Figure 2 shows an example of an isothermal desorption of a well ordered Xe monolayer, monitored at $\Theta_f = 0°$. Data were taken by pulse counting over discrete time intervals of constant width, the width chosen being dependent upon the desorption rate. Due to the fact that the differentially pumped and highly collimated detector looks at only a small spot on the crystal, we did not have to worry about desorption from the manipulator or make corrections for pumping speed, as the amount of Xe entering the ionizer was small. A series of these experiments were done for temperatures from 63 to 69 K. All of the spectra show the same overall shape; desorption appears to be zeroth order, or nearly so, until approximately 90% of the Xe has desorbed, at which point the desorption rate begins rapidly decreasing with decreasing coverage. The gentle downward slope in the nearly zeroth order regime is found in most of the data, and has also been observed for Xe/W(110) by Opila *et al.*[25]

We can write the rate equation in the general form

$$-\frac{\partial\theta}{\partial t} = \theta^n k_n = \theta^n \nu_n \exp\left(\frac{-E_a}{RT}\right), \quad (1)$$

where θ is the coverage, n is the order of the desorption, k_n is the rate constant, ν_n is the frequency factor, and E_a is the activation energy for desorption. The zeroth order rate constant k_0 was determined from the relation

$$Ci_{\rm ms} = -\frac{\Delta\Theta}{\Delta t} = k_0, \quad (2)$$

where $i_{\rm ms}$ is the mass spectrometer signal, and C is a proportionality constant. The only other information needed was θ_0, the saturation coverage of the Xe monolayer. This was determined to be 6.02×10^{14} atoms/cm^2, using a lattice constant of 4.38 Å. A plot of $\ln(k_0)$ vs $1/T$ is shown in Fig. 2. The calculated activation energy is 4.77 ± 0.10 kcal/mol, and the preexponential is $(1.2\pm1.0)\times10^{28}$ atoms/(cm^2 s).

The portions of the spectra with decreasing desorption rate were fit with an exponential, assuming first order kinetics, and k_1, the first order rate constant, was determined from the relation

$$i_{\rm ms} = C'\exp[-k_1(t-t_1)], \quad (3)$$

where t is the time, t_1 is some time at which desorption is first order, and C' is a proportionality constant dependent upon t_1 and the sampling rate. This procedure gave a good fit to the data over the last approximately 70% of the region. A plot of $-\ln(k_1)$ is also shown in Fig. 2, giving an activation energy of 4.95 ± 0.25 kcal/mol, and a preexponential of $(2\pm4)\times10^{15}$ s^{-1}.

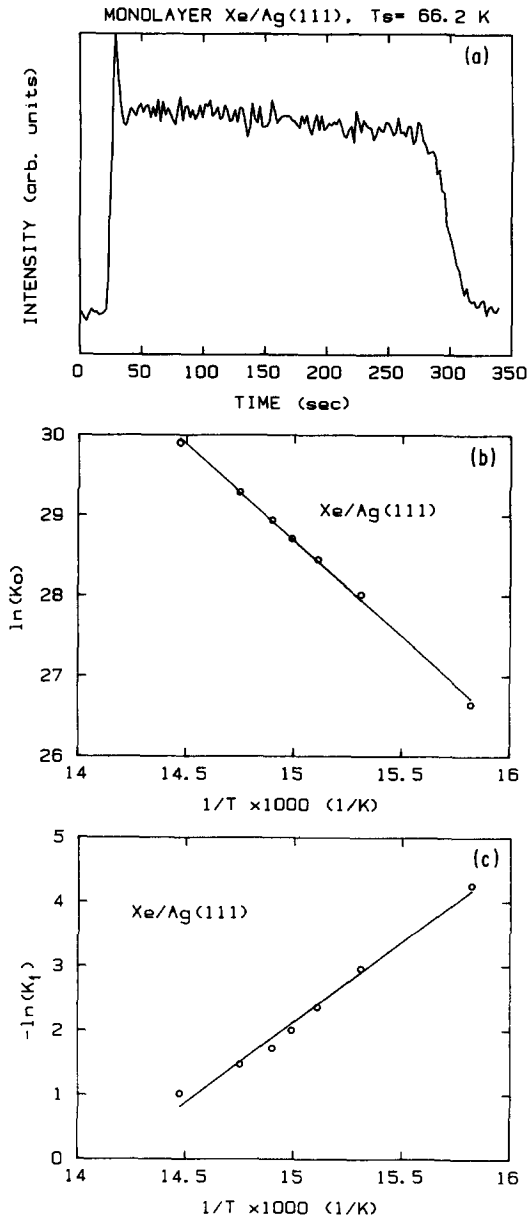

FIG. 2. (a) is an example of an isothermal desorption spectrum of a Xe monolayer physisorbed on Ag(111). It shows the general features of all of the isothermal desorption runs: the desorption rate is constant, or zeroth order, until approximately 90% of the Xe has desorbed, where it then begins to exponentially decrease, which is the first order regime. The signal spike at the beginning of the desorption is caused by a slight initial temperature overshoot due to the response time of the temperature controller. (b) is an Arrhenius plot for the zeroth order desorption, and (c) is an Arhennius plot for the first order desorption.

These error bars are 95% confidence intervals estimated from the fits of $\ln(k)$ vs $1/T$. There is also a systematic error due to the uncertainty in the temperature calibration (±3 K). Within this variation of temperature, the values of E_a are within 0.4 kcal/mol and ν_n are within an order of magnitude.

Behm *et al.*[29] have also observed zeroth order kinetics for Xe monolayer/Ag(111), although their derived value of $E_a = 5.2$ kcal/mol is somewhat larger than ours. Similar

behavior was observed for Xe/W(110) by Opila and Gomer,[25] their activation energies were about a kcal/mol smaller, and the transition from zeroth to first order kinetics occurred where approximately 70% of the monolayer had desorbed. One explanation for zeroth order desorption is given both by Opila and Gomer, and by Venables and Bienfait.[30] This mechanism proposes an equilibrium between both a dense ordered phase and a more dilute random phase, plus an equal desorption rate from both phases. As Opila and Gomer point out, this implies an equivalent sticking probability for both phases. Though this may appear unlikely, it seems to be nearly true for the Xe/Ag(111) system. This was checked by adjusting the temperature of the crystal so that it was slightly below the monolayer desorption temperature with the dosing beam on. The Xe signal was then monitored with the mass spectrometer. This signal was nearly zero until the time to deposit a complete monolayer had elapsed, when the Xe signal increased quite suddenly. The desorption then becomes first order when the dense ordered phase is depleted. However, the above mechanism requires that the activation energy should be equal for both the zeroth and first order regions. Within our experimental uncertainty, this appears to be true, as is the case for the data of Opila and Gomer.

To investigate the presence of ordered Xe islands, we did an isothermal desorption experiment where both the Xe desorption signal and a nonspecular overlayer He diffraction peak were *simultaneously* monitored by rapidly switching the quadrupole mass tuning. Only coherent scattering from ordered islands of Xe will contribute to the observed diffraction signal. The result of this "time-resolved diffraction" experiment is shown in Fig. 3, where the $(\bar{1}\,\bar{1})$ diffraction peak at $\Theta_i = 70°$ was monitored with a 64 meV He beam. It is apparent that ordered islands are present while the desorption kinetics are zeroth order. Noting where the diffraction precisely vanishes is ambiguous, due to signal-to-noise considerations. The He diffraction signal does seem to disappear

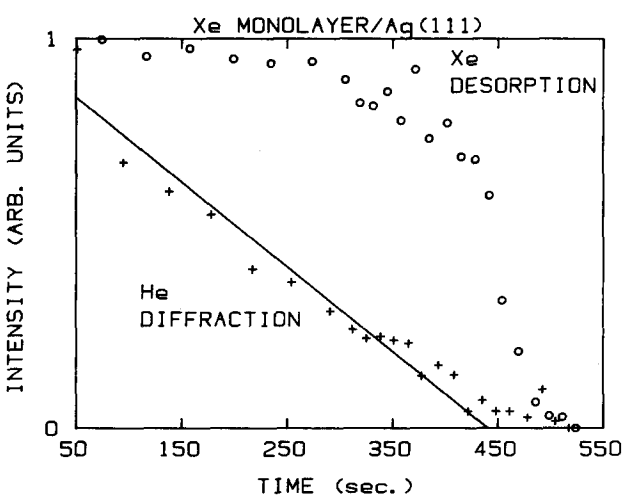

FIG. 3. Plot of data for an experiment where both the He diffraction (crosses) and Xe desorption (circles) were *simultaneously* measured for a monolayer physisorbed on Ag(111). He diffraction is from the $(\bar{1}\bar{1})$ rod along the $\langle 11\bar{2}\rangle$ azimuth, with a 64 meV beam. Surface temperature was 64.2 K. The straight line through diffraction data points is a least-squares fit for values greater than the background noise.

at the transition region between zeroth and first order desorption kinetics, however. The decay of the diffraction data is linear in time, and is reasonable if the detector is viewing most of the diffraction peak. Let n_x and n_y be the dimensions for an ordered island, in number of scatterers in the x and y directions. The peak height of the diffraction signal will be proportional to $(n_x n_y)^2$, and the width will be proportional to $(n_x n_y)^{-1}$, so the integrated intensity (width times height) will be proportional to $(n_x n_y)$. Since the coverage is decreasing linearly with time during zeroth order desorption, a straight line will result. Deviations will occur when the angular width of the diffraction peak is wider than the acceptance angle of the detector. Since the width of the diffraction peak is a measure of the island size, it would be interesting to measure this and see if the islands are constant in number, or whether larger numbers of smaller islands are constantly forming. Since this requires making angular scans with the detector, it is more easily done with a slow dosing rather than a desorption experiment. One interesting conclusion that is suggested by this time-resolved diffraction experiment, is that the zeroth order kinetics can be associated with the existence of ordered rare gas islands. Although not conclusively demonstrated, due to the width of the zeroth to first order desorption kinetics transition, the first order region could be due to the presence of a disordered phase. Higher quality measurements of this phenomenon are warranted.

It is also interesting to note the results of Unguris *et al.*,[6] and Poelsma *et al.*[31] Using LEED, Unguris *et al.* observed the intensity of diffraction when a Ag(111) crystal was exposed to a constant flux of Xe. At low coverage, they observed attenuation of the specular beam, and observed diffraction from ordered Xe only after the coverage was several percent of a monolayer. This indicates that only a randomly adsorbed phase exists at low coverage. Poelsma *et al.* observed the intensity of specularly reflected He as a function of time of exposure of a Pt(111) crystal to a low pressure Xe dosing beam. A break in the intensity of scattered He vs exposure curves was seen when the coverage (assuming a sticking probability of 1) was only a few percent of monolayer saturation coverage. They attribute this result to the formation of Xe islands. We never dosed the Ag(111) crystal at low enough rates to reproduce these experiments. However, we did use short consecutive doses of Xe, and looked for He diffraction from the partial Xe overlayer between each dose. The result is shown in Fig. 4. This experiment was done at 24 K, while monitoring the $(\bar{1}\,\bar{1})$ diffraction peak at $\Theta_i = 70°$ with a 64 meV He beam. The surface temperature was well below that at which observable Xe desorption occurs, even with the dosing beam off. Observable diffraction is seen even when coverage would correspond to only approximately 17% of a full monolayer.

We also observed the elastic scattering of He from the Ag(111) surface partially covered with 6% Xe and 11% to 14% Xe, as determined by the integrated area of the Xe thermal desorption spectra. The results can be compared with the formula of Poelsma *et al.*[32]:

$$\frac{I_{00}}{I_0} = 0.72(1-\Theta)^{n_s \Sigma_{Xe}}, \tag{4}$$

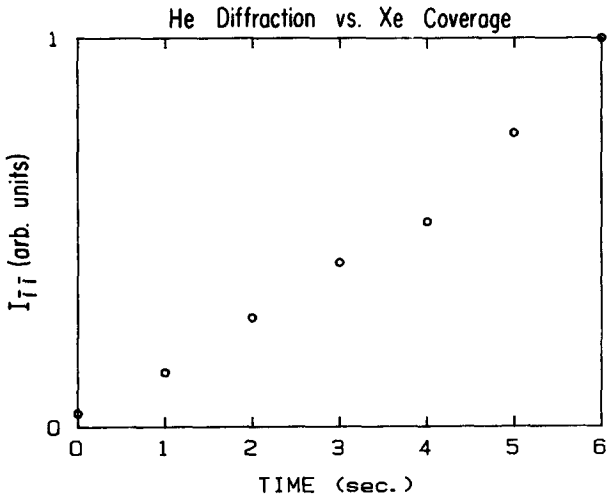

FIG. 4. Relative signal for a 64 meV He beam diffracting from the $(\bar{1}\bar{1})$ rod of Xe monolayer islands as a function of Xe coverage on Ag(111). Diffraction is along the $\langle 11\bar{2}\rangle$ azimuth, and $T_s = 24$ K (T_s is the surface temperature). Data are for consecutive 1 s doses, with 6 s being nearly a full monolayer. Since the sticking coefficient is nearly unity at this temperature, each 1 s dose represents an equal amount of Xe deposited on the surface.

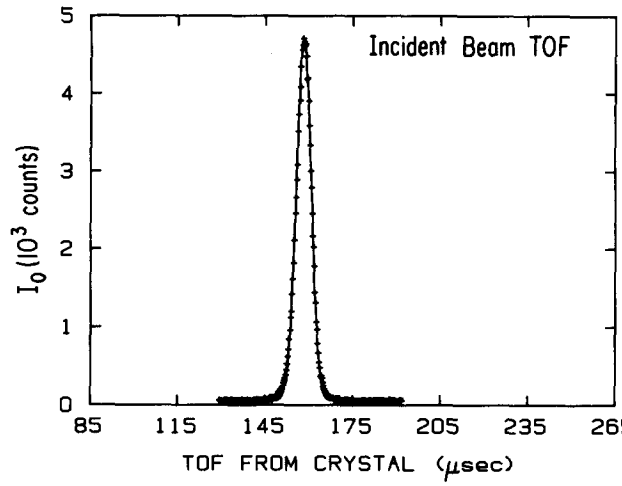

FIG. 5. TOF spectrum of the incident 18 meV He beam. The solid line is a Gaussian fit to the data.

where Θ is the relative coverage of Xe, n_s is the number of adsorption sites per unit surface area (6.02×10^{-2} Å^{-2}), Σ_{Xe} is the scattering cross section for adsorbed Xe, and the prefactor of 0.72 is I_{00}/I_0 for our clean Ag crystal at 24 K. For the coverages greater than 11%, the intensity measurements were closely matched by using a value for Σ_{Xe} of 20 Å^2($I_{00}/I_0\approx0.6$), which corresponds to island growth,[31] rather than a value for Σ_{Xe} of 120 Å^2, which would correspond to random adsorption, and gives a value of $I_{00}/I_0\approx0.25$. The value of I_{00}/I_0 for 6% coverage was intermediate to those determined for isolated atom and island formation, using the above two values for Σ_{Xe}. For the larger coverages, the results were independent of whether the Xe was simply deposited at $T_s = 24$ K, or grown at this temperature and annealed at 56 K for several minutes. These attenuation measurements for Xe coverages greater than 11% of a monolayer and a surface temperature of 24 K indicate that the Xe probably exists as islands on the Ag(111) surface, rather than as a random phase. This is consistent with the presence of diffraction from the Xe overlayers at these coverages.

INELASTIC SCATTERING: TRANSITION ENERGIES

The first rare gas studied was Xe. Of the incident angles initially tried, $\Theta_i = 45°$ had good intensities for interactions with phonons in the first SBZ, and reasonably good parallel momentum resolution. At $\Theta_i = 35°$, while the intensity was good, it suffered somewhat from a larger Debye–Waller attenuation, and poorer parallel momentum resolution. (The detector has constant angular resolution, so that parallel momentum resolution is a trigonometric function of the incident angle, and gets worse at more normal incident angles.) Ar and Kr also showed good inelastic scattering intensities at $\Theta_i = 45°$, so for all three rare gases, most of the experiments were done at this angle of incidence.

Figure 5 shows a time-of-flight (TOF) spectrum of an

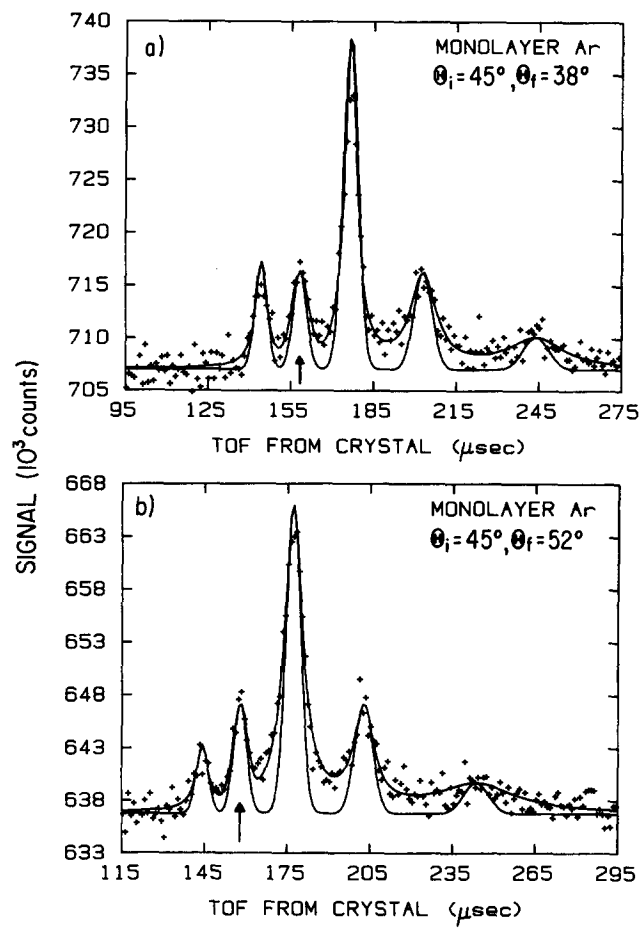

FIG. 6. Some TOF spectra of an 18 meV He beam scattering from an Ar monolayer physisorbed on Ag(111), taken along the $\langle 11\bar{2}\rangle$ azimuth, with $T_s = 22.5$ K, and 1 h of signal averaging. Arrows indicate the position of the elastic channel. Solid lines that nearly fit the data points are from the energy-broadened simulation, the narrower curves are the simulation without energy broadening (see the text). In the case of the nonenergy-broadened simulations, the peak heights have been scaled to that of the broadened simulations, to show the difference in the widths. The same format has been used for Figs. 7, 8, 16, and 30. For the peak to the right of the elastic channel, corresponding to a transition involving creation of a normal phonon, $Q/K(\bar{M}) = -0.96$ in (a), and $Q/K(\bar{M}) = -0.04$ in (b). [$K(\bar{M})$ is the position of the zone edge in reciprocal space, $2\pi/a\sqrt{3}$, where a is the lattice constant.]

incident 18 meV He beam. This can be contrasted with Figs. 6–8, which show some TOF spectra for this beam scattered from Ar, Kr, and Xe monolayers, respectively. These were all taken at $\Theta_i = 45°$ in the $\bar{\Gamma}$–$\bar{M}$ direction, and with Θ_f well away from the angular positions of the elastic features. All show one feature that is fast relative to the elastic channel, corresponding to phonon annihilation, and two or three slower features, corresponding to phonon creation. For the Xe monolayer, only two slower features are seen at $\Theta_i = 45°$. There is also a feature at the position of the elastic channel. For final angles well away from an elastic feature, this is probably due to elastic scattering from crystal defects. At final angles that fall within about 0.5 of the SBZ of an elastic feature, there are contributions due to the finite angular spread and size of the incident beam, the finite acceptance angle of the detector, and broadening of the elastic feature due to the finite coherence length of the surface. When the elastic feature is other than the specular, there is a further contribution that comes from the dispersion of the incident velocity distribution. When TOF spectra were taken at the specular angle, the appearance of the spectrum was similar to that of the incident beam, but had a slightly larger FWHM. An example is shown in Fig. 8(f). To get a qualitative feel for the intensities of the inelastic scattering, refer to Fig. 1. The data for Figs. 6–8 were taken at final angles between the positions of the elastic features.

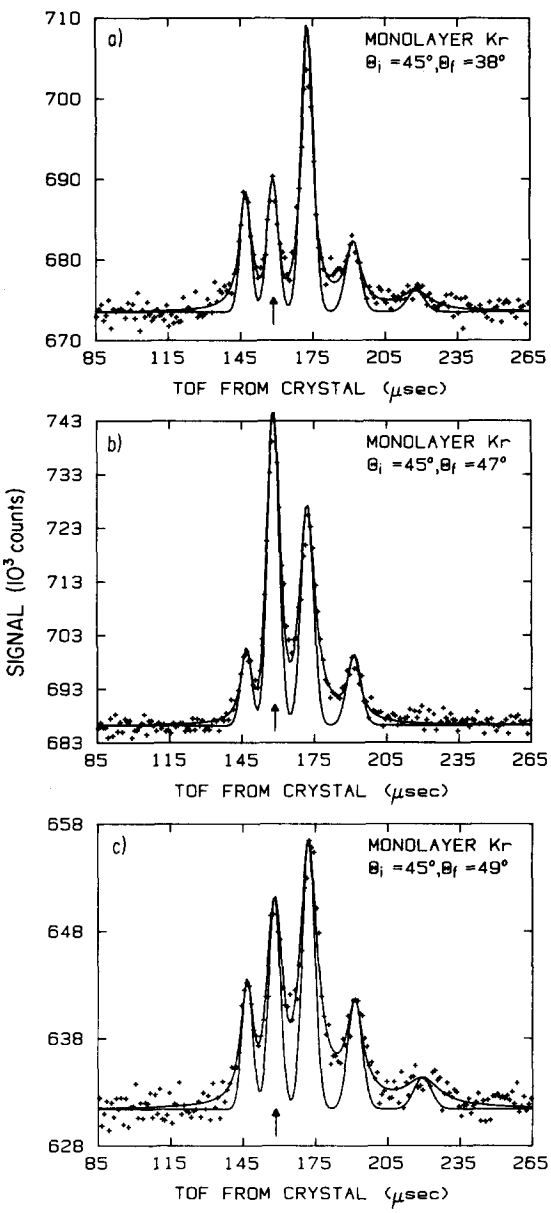

FIG. 7. Some TOF spectra of an 18 meV He beam scattering from a Kr monolayer physisorbed on Ag(111), taken along the $\langle 11\bar{2}\rangle$ azimuth, $T_s = 24$ K, and 1 h of signal averaging. For the peak to the right of the elastic channel, corresponding to a transition involving creation of a normal phonon, $Q/K(\bar{M}) = -0.93$ in (a), $Q/K(\bar{M}) = -0.24$ in (b), and $Q/K(\bar{M}) = -0.12$ in (c). For an explanation of the solid lines, see Fig. 6.

Preliminary data analysis consisted of fitting the spectra using a nonlinear least-squares routine to determine the time of flight of the maxima for the various features. A TOF spectrum of the specular, and occasionally other elastic features, was taken before and after each inelastic scattering spectrum. The comparison of the flight times for the elastic scattering as compared to the straight-through beam was used to confirm that the crystal was properly aligned. The difference in flight times was always less than 0.5 μs, close to the time resolution of the experiment. Any slight difference was largely corrected for by using the elastic TOF in computing the phonon energies. Flight times, referenced to the elastic TOF, were then used to determine the phonon energy, using the conservation of energy,

$$E_f = E_i \pm n\hbar\omega(\mathbf{Q}) , \tag{5}$$

where E_i and E_f are the incident and final energies of the scattered He, $\omega(\mathbf{Q})$ is the phonon frequency, and n is the number of phonons created or annihilated. With the energy of the scattered He, and the incident and final scattering angles, the conservation of crystal momentum condition allows the parallel momentum exchange to be calculated,

$$\mathbf{K}_f = \mathbf{K}_i + \mathbf{G} \pm \mathbf{Q} , \tag{6}$$

where $\mathbf{K}_i$ and $\mathbf{K}_f$ are the incident and final parallel momentum of the scattered He, $\mathbf{G}$ is a reciprocal lattice vector, and $\mathbf{Q}$ is the parallel momentum transfer due to interaction with surface phonons. (As is the usual practice, upper case letters refer to vectors in the plane of the surface, lower case letters refer to vectors which include a component perpendicular to the surface.) Using Eq. (5), the following can be derived:

$$n\hbar\omega = E_f - E_i = (Mv_i^2/2)[(1 + \{v_i \Delta t_{xd}/l_{xd}\})^{-2} - 1] , \tag{7}$$

where Δt_{xd} is the shift in the TOF maximum of the inelastic scattering as compared to the elastic scattering, l_{xd} is the crystal to detector distance, and M is the mass of a He atom. The incident velocity v_i can be determined either by the position of the elastic time of flight, or somewhat more accurately by using the deconvolution program described in the next section. Using the maxima of the spectra for this analysis is not strictly correct, since the velocity distribution has a finite width, and the distribution for a number density detector is

$$n(v) = Cv^2 \exp\{-[(v - v_0)/\alpha]^2\} , \tag{8}$$

where α is the velocity width, C is a proportionality constant, and v_0 is the stream velocity. The difference needed is between the stream velocity of the incident and scattered He,

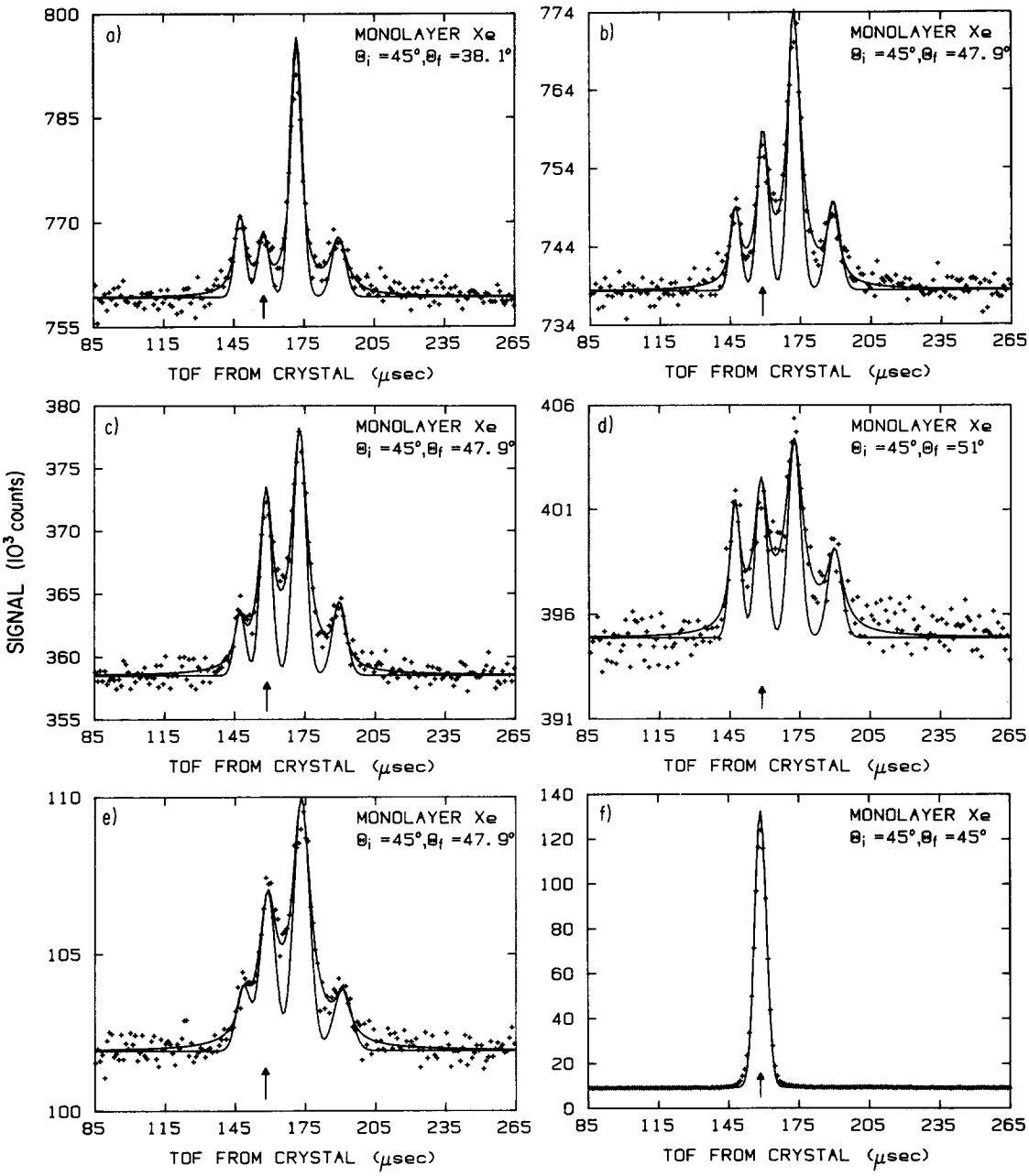

FIG. 8. Some TOF spectra of an 18 meV He beam scattering from a Xe monolayer physisorbed on Ag(111), taken along the $\langle 11\bar{2}\rangle$ azimuth, $T_s = 24$ K, and 1 h of signal averaging. For the peak to the right of the elastic channel, corresponding to a transition involving creation of a normal phonon, $Q/K(\bar{M}) = -0.99$ in (a), $Q/K(\bar{M}) = -0.19$ in (b), $Q/K(\bar{M}) = -0.20$ in (c), $Q/K(\bar{M}) = -0.02$ in (d), and $Q/K(\bar{M}) = -0.20$ in (e). The spectra in (a)–(d) were taken with a 350 Hz chopper frequency. (b) and (c) show spectra for two different monolayers, with about six months elapsing between the two experiments, to show the reproducibility of the results. The spectrum shown in (e) was taken with a 200 Hz chopper frequency, which causes the peaks to be broader. For explanation of the solid lines, see Fig. 6. (f) shows the TOF spectrum for the specular reflection, using a 350 Hz chopper and about a minute of signal averaging. The solid line is a Gaussian fit to the data.

which is not quite given by the position of the maxima. However, for the narrow velocity spread of the incident He beam, this error is negligible.

With the final energy determined, Eq. (6) can be used to calculate the parallel momentum transfer

$$\mathbf{Q} = (2M/\hbar^2)^{1/2}\left[(\sqrt{E_f})\sin(\Theta_f) - (\sqrt{E_i})\sin(\Theta_i)\right] - \mathbf{G}\,. \tag{9}$$

Figures 9–11 show the results of this analysis for the three rare gas monolayers. In these figures, the signs of the $\mathbf{Q}$ and E are with respect to the scattered He. As previously mentioned, much of the data was taken at $\Theta_i = 45°$. We took at least enough spectra at this incident angle to follow the large energy loss feature, the peak immediately to the right of the elastic channel in Figs. 6–8, from the center to the edge of the first SBZ. This was done by varying the detector angle while keeping the incident angle fixed. The inelastic processes observed were then determined by the scan curve

$$\mathbf{k}_i^2 \pm 2nM\omega(\mathbf{Q})/\hbar^2 - (\mathbf{K}_i + \mathbf{G} \pm \mathbf{Q})^2/\sin^2(\Theta_f) = 0\,. \tag{10}$$

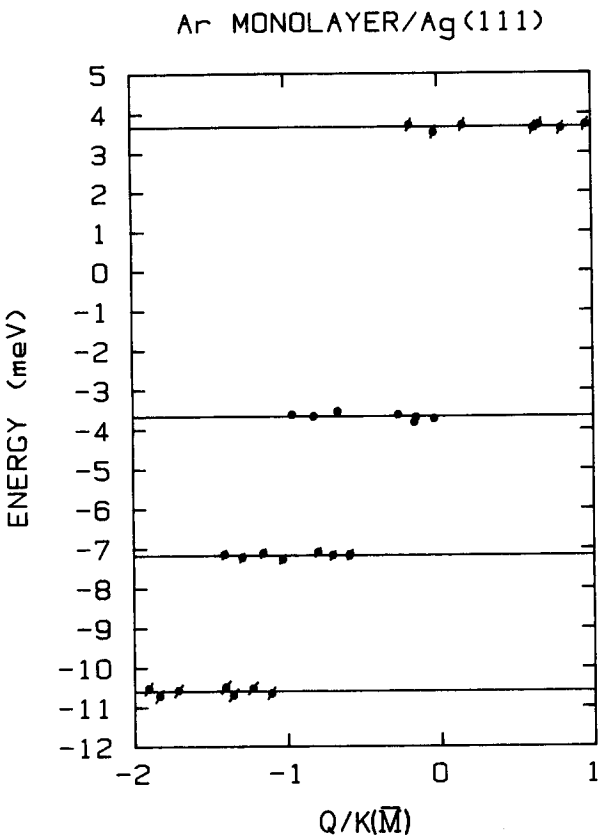

FIG. 9. Energies of the observed inelastic transitions along the $\langle 11\bar{2}\rangle$ azimuth for the Ar monolayers physisorbed on Ag(111), as a function of parallel momentum transfer. Solid lines represent the average of the data points.

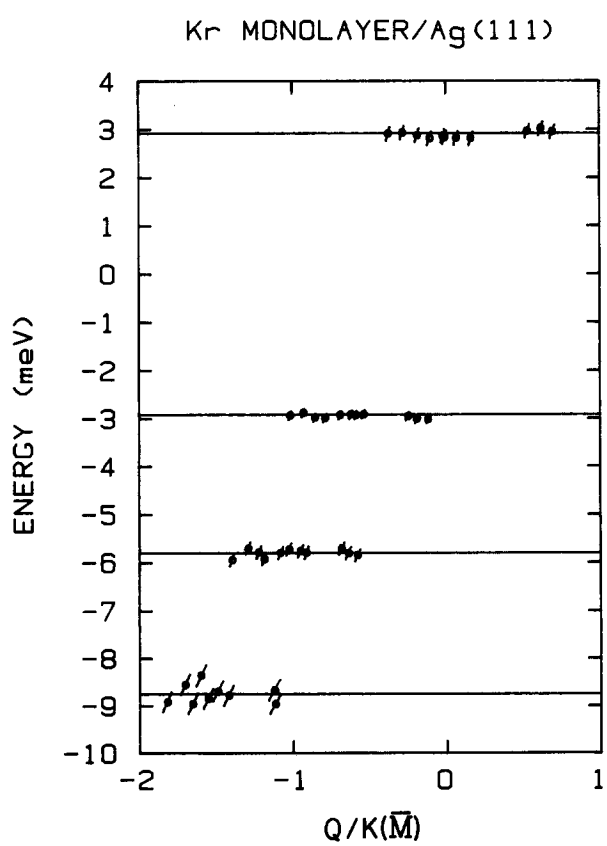

FIG. 10. Same as Fig. 9, for the Kr monolayers.

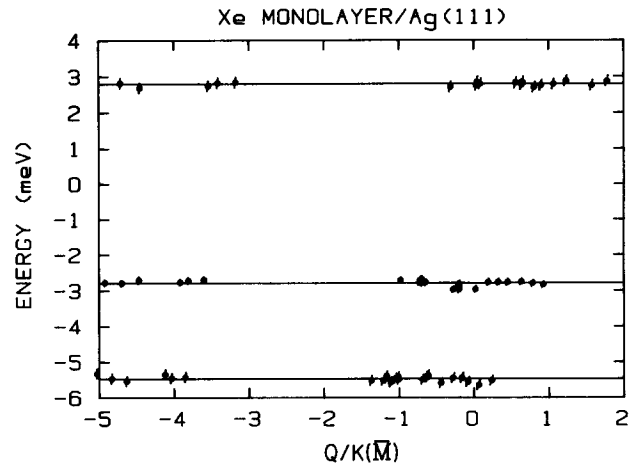

FIG. 11. Same as Fig. 9, for the Xe monolayers.

The first observation is that all of the inelastic scattering is dispersionless, within our experimental error. This is indicative of Einstein oscillator behavior, where the adsorbed atoms are independently vibrating perpendicular to the surface in the rare gas–Ag holding potential. This behavior has been observed for rare gas monolayers physisorbed on other metal surfaces,[14–17] and inferred from the thermal attenuation of H scattering from a Xe monolayer adsorbed on graphite.[33] The energies of the interactions are given in Table II.

That there is a mode, labeled $SP_{\perp}$, with perpendicular polarization implies that the rare gas atoms are sensitive only to the influence of the laterally averaged potential, and not to the higher order Fourier components of the (smooth) Ag(111) substrate. That this mode is dispersionless, at least within our experimental error, can be qualitatively explained. At short wavelengths, where adjacent adsorbate atoms are moving in opposite directions, there is an additional restoring force from the lateral interactions between adatoms. For long wavelengths, neighboring atoms are moving almost in unison, so that it would appear that there might be some dispersion in this mode. However, it is easy to show that the restoring force due to adjacent atoms will always be small. Let the magnitude of the rare gas atom's motion perpendicular to the surface be denoted by z, and the Ag–rare gas force constant be k_{Ag}. Then the restoring force is $F = -k_{Ag}z$. Let the surface lattice constant for the rare gas be y. Considering only the nearest neighbor interactions between two rare gas atoms whose motions are 180° out of phase, the additional restoring force perpendicular to the surface is $F_z = -2k_{RG}\{[y^2 + (2z)^2]^{1/2} - y\}$, where k_{RG}

TABLE II. Average values for the energies of the inelastic scattering transitions. Plus or minus refers to phonon annihilation and creation, respectively, with the number referring to the number of phonons created or annihilated. The numbers in parentheses are 95% confidence intervals.

Adsorbate	+1	−1	−2	−3
Ar	3.67(0.15)	3.67(0.08)	7.18(0.11)	10.60(0.15)
Kr	2.92(0.14)	2.92(0.09)	5.80(0.13)	8.75(0.21)
Xe	2.79(0.15)	2.79(0.09)	5.47(0.14)	···

is the rare gas–rare gas force constant. Since z is small, on the order of 0.1 Å (see Debye–Waller analysis below), the quantity in parentheses can be expanded. The result is that $F_z \approx -4k_{RG}z^2/y$, which will be much smaller than the restoring force due to the Ag–rare gas interaction.

Another question is why only one mode is observed. If there is no coupling to the substrate vibrations, then there are three modes, which have been calculated by Gibson *et al.*[21] and O'Shea *et al.*[22] Besides the dispersionless mode, there is a transversely polarized mode and a longitudinally polarized mode, and both exhibit dispersion. The transversely polarized mode is perpendicular to the scattering plane, so that even if it coupled with the incoming He beam, the scattering would be out of plane and not observed. However, inelastic scattering involving the longitudinal mode would be in the scattering plane, yet none is observed, even at the more glancing incident angles. He scattering measures the corrugation of the surface potential at the distance of closest approach, which may be several angstroms above the surface. The intensity of the inelastic scattering is related to the perpendicular displacement of the vibrational mode, just as the intensity of elastic scattering is related to the perpendicular corrugation of the static lattice.[34] The $SP_\perp$ mode involves displacements perpendicular to the surface, whereas the longitudinal mode does not. Therefore, inelastic scattering is most sensitive to the former. We note, however, that in many other systems involving both clean and adsorbate covered surfaces, longitudinal modes will not be exclusively polarized in the surface plane, but will have hybrid character leading to displacements normal to the surface. Such modes will be observable with inelastic He scattering, as exemplified by clean Ag(111), which is briefly discussed later in this paper.

Another feature of the inelastic scattering is that all possible combinations of $\Delta\mathbf{Q}$ and ΔE are observed, as well as umklapp phonons. This is the same behavior seen for the corrugated surfaces of LiF, NaF, and KCl.[35] Umklapp phonons are also observed on the corrugated Ag(001)-$c(2\times2)$Cl surface.[36] In contrast, umklapp phonons are not observed on the relatively smooth surfaces of transition metals,[36–38] and there is a preferred sign for $\Delta\mathbf{Q}$ for a particular sign of ΔE. This latter observation is, however, at least partially due to the kinematics of the scattering. The same conclusion was reached by Kern *et al.*[39] Figure 12 shows the inelastic transitions we observed for 18 meV He scattering from Ag(111) along the $\langle 11\bar{2}\rangle$ azimuth. For the Rayleigh surface mode of the Ag, we observed *all* possible values of $\Delta\mathbf{Q}$ and ΔE near the zone center allowed by the scan curves. Since the rare gas monolayer modes are dispersionless, there is no problem with the scan curves intersecting a mode with any sign of $\Delta\mathbf{Q}$ and ΔE. The connection between surface corrugation and the observation of umklapp phonons is expected, because the strength of the inelastic scattering should be related to the intensity of the nearest elastic feature.[34]

The observed inelastic scattering from rare gas overlayers also shows features that are nearly integral multiples of the fundamental frequency, as shown in Table II. This same behavior has been seen for rare gas monolayers on other metal surfaces.[14–17] These higher order features are not

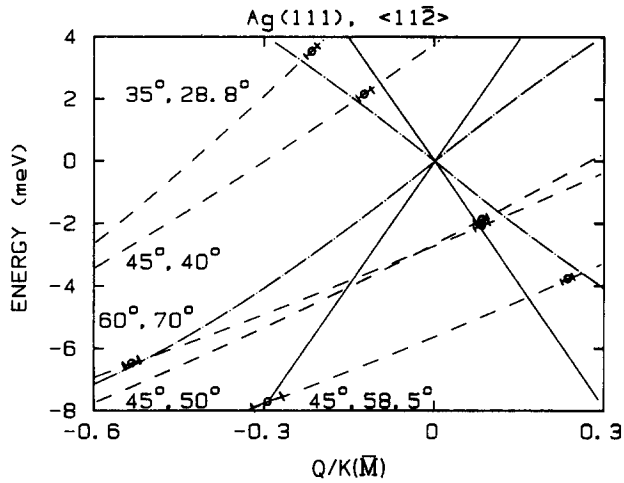

FIG. 12. Energies of the observed inelastic transitions for an 18 meV He beam scattering from Ag(111) along the $\langle 11\bar{2}\rangle$ azimuth, with $T_s = 24$ K. Dot–dash lines are the position of the Rayleigh wave of the Ag, and the solid lines are the approximate position of the pseudomode. Dashed lines are the scan curves. The two numbers which label each scan curve are the incident angle and detector angle, respectively.

seen in scattering from clean metal surfaces, and are certainly not as pronounced in scattering from rare gas multilayers.[21,40] In the latter case, multiple inelastic features can possibly be explained by interaction with more than one phonon mode. In the case of the monolayers, the inelastic features involving higher energy exchange may be due to two possible processes. The first, which we will call multiphonon, would come about if the impinging He atom interacts inelastically with more than one adsorbed rare gas atom. When a mode exhibits dispersion, these multiphonon interactions will result in a broad background for the TOF spectra. However, a dispersionless mode will still have discrete peaks. The second, which we will call overtone scattering, occurs if there is a binary collision, and the adsorbed rare gas changes its vibrational state by more than one level.

One way to differentiate between them is to construct a Ag–rare gas potential, to see if the level spacing is harmonic. The technique of selective adsorption can be used to determine the gas–Ag surface potential for light atoms. However, this technique is not applicable for heavy atoms. Instead, the inelastic scattering gives useful information for an alternate method of deriving the potential. Since the $SP_\perp$ mode has the rare gas atoms vibrating in this potential well, the frequency gives the force constant and therefore the curvature of the potential well at its minimum. Using this information, an experimental value for the well depth,[41] and a theoretical value for C_3,[42] we derived an exponential-3 parametrization of the holding potential

$$V(z) = A\exp[-\beta(z-z_0)] - C_3/(z-z_0)^3, \quad (11)$$

where z_0 is the position of the reference plane. The values are given in Table III. No saturation term has been included, such as that suggested by Nordlander and Harris,[43] so that the parametrization is not valid for small z. For Ar, Kr, and Xe monolayers, these potentials are nearly harmonic up to $n = 4$ or 5, so that the possibility of overtones is not ruled out. An examination of Table II shows that there is a small

TABLE III. Parameters for the exponential-3 rare gas–Ag holding potential (see the text). Values of D are from Bruch (Ref. 41) and values of C_3 are from Zaremba and Kohn (Ref. 42).

Adsorbate	A (meV)	β (Å^{-1})	D (meV)	C_3 (meV Å^3)
Ar	18 806	2.446	66	1623
Kr	21 556	2.407	108	2263
Xe	31 724	2.443	172	3277

discrepancy between the values of the higher energies and an integral multiple of the lowest energy, at least for Ar and Xe. For Ar, the differences are 0.16 meV ($2\times3.67=7.34$) and 0.41 meV ($3\times3.67=11.01$). For Xe, the difference is 0.11 meV ($2\times2.79=5.58$). Only for the case of the triple loss for Ar is this difference significant. It seems most probable that nonbinary scattering should be nearly integral multiples of the lowest energy, and any deviation from integral multiples should indicate overtones, the difference arising from anharmonicity in the Ag–rare gas potential. If this is the case Ar, with the smallest lattice constant of the three rare gas adsorbates, should be the least likely to have strictly binary collisions, have the largest contribution from nonbinary interactions, and have energies closest to being integral multiples of one another. It is possible that there is a combination of these two processes. The other consideration is that lateral interactions between the adsorbate atoms may have some small effect on overtone frequencies.

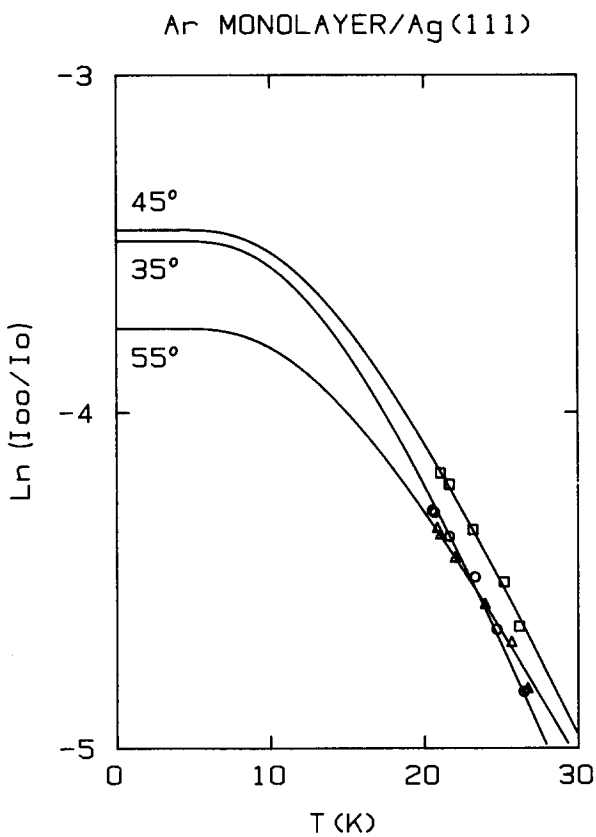

FIG. 13. The logarithm of the specular intensity divided by the incident intensity plotted vs the surface temperature for an 18 meV He beam scattering from an Ar monolayer physisorbed on Ag(111) at three different incident angles. See the text for an explanation of the solid lines.

Before proceeding with a discussion of the inelastic scattering probabilities, the thermal attenuation of the scattering has to be determined. The experiments to measure this effect involved measuring the specular intensity as a function of surface temperature at several incident angles. Figures 13–15 show the results for Ar, Kr, and Xe monolayers, where I_{00}/I_0 is plotted vs the surface temperature, I_{00} and I_0 being the reflected and incident beams, respectively. This data is usually fit to an equation like that used for x rays[44] and neutron scattering,[45]

$$I_{00}/I_0 = P_{\rm el}\exp(-\langle \Delta\mathbf{k}\cdot\mathbf{u}_{\rm eff}\rangle)^2 , \quad (12)$$

where $P_{\rm el}$ is the elastic probability, $\Delta\mathbf{k}$ is the momentum transfer, and $\mathbf{u}_{\rm eff}$ is the effective displacement of the surface atoms. For specular reflection, this reduces to

$$I_{00}/I_0 = P_{\rm el}\exp(-\Delta k_z^2\langle u_z^2\rangle) , \quad (13)$$

where $\langle u_z^2\rangle$ is the mean-square displacement of an atom perpendicular to the surface. According to the criteria of Levi and Suhl,[46] the collision of an 18 meV He atom with these surfaces is rather slow, and so this simple analysis could be incorrect. Also, it neglects the Armand effect[47] in assuming only collisions with a single surface atom, which should become increasingly important going from Xe to Ar, which is the direction of decreasing lattice constant.

Since the surface atoms are behaving as Einstein oscillators, an analysis like that of Ellis *et al.*[33] was used. The Einstein oscillator approximation gives

$$\langle u_z^2\rangle = (\hbar/2M\omega)\coth(\hbar\omega/2k_bT) , \quad (14)$$

where M is the mass of the surface atom, and k_b is Boltzmann's constant. The lowest energy in Table II was used to

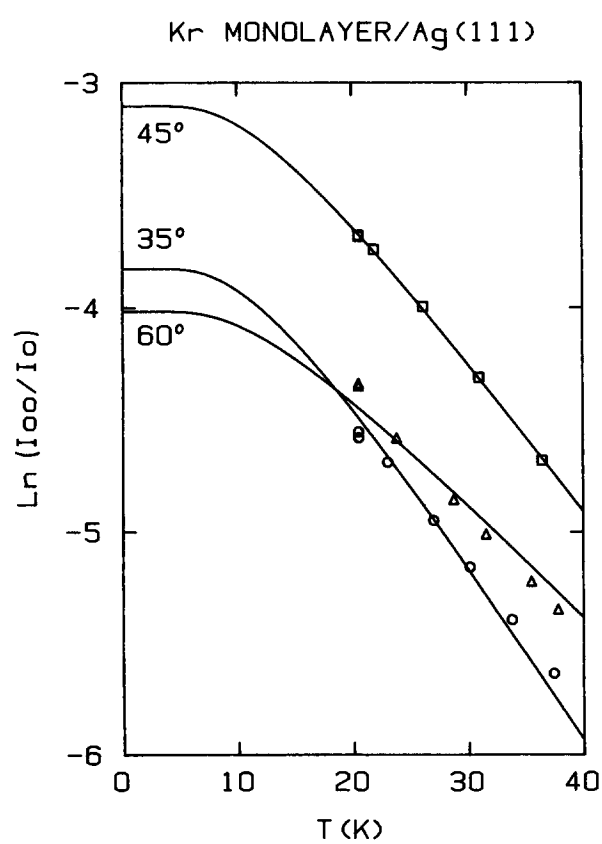

FIG. 14. Same as Fig. 13, for a Kr monolayer.

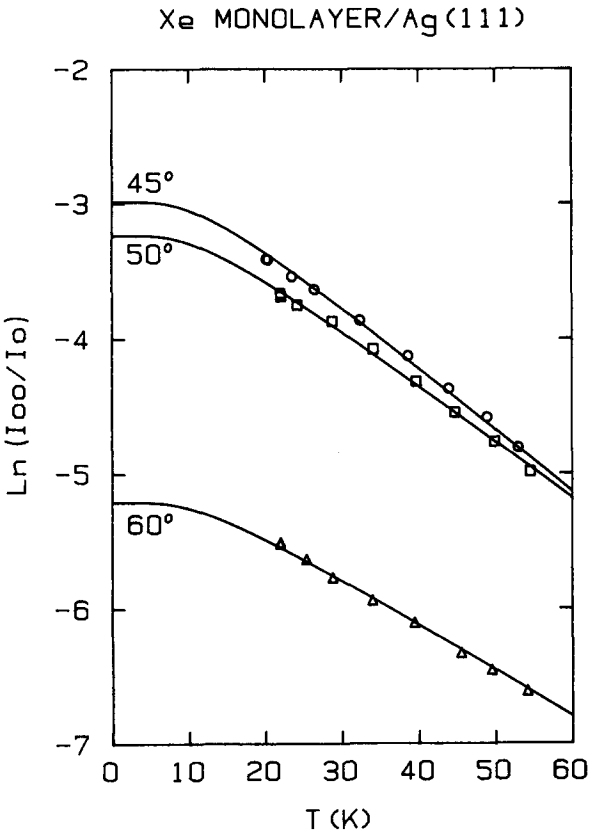

FIG. 15. Same as Fig. 13, for a Xe monolayer.

calculate ω for each rare gas monolayer. For the momentum transfer, the Beeby correction was used,[48] which takes into account acceleration of the He atom in the attractive well, so

$$\Delta k_z = k_i[\cos^2(\Theta_i) + D/E_i]^{1/2} + k_f[\cos^2(\Theta_f) + D/E_f]^{1/2}, \tag{15}$$

where D is the well depth, k_i is the mean incident wave vector, k_f is the mean final wave vector, and E_i and E_f are the mean initial and final energies. For the specular, $\Theta_i = \Theta_f$, $k_i = k_f$, and $E_i = E_f$.

The results were fit using Eqs. (13)–(15), with D and P_{el} used as adjustable fitting parameters. The results are shown as the solid lines through the data points. The calculated values of D are 12.61 meV for Ar, 9.46 meV for Kr, and 8.55 meV for Xe. Xe fits this model, using a single value of D for all of the incident angles, the best of the three rare gases. The data for Ar and Kr fits somewhat less well when only one value of D is used. However, if D is allowed to vary for each incident angle, the fits are improved. The ranges for D in this case are 11.0–13.6 meV for Ar, 6.5–12.5 meV for Kr, and 7.7–9.1 meV for Xe. In all cases, the value of D increases at more glancing incidence angles. To really test this Debye–Waller parametrization, it would be necessary to cool down past the region where the curves become horizontal, but these temperatures were unobtainable with our apparatus. It is of interest that the values obtained for the well depths are not entirely unreasonable. For all of the rare gases, they are only a few meV deeper than those calculated by Chung *et al.*[49]

Though this Debye–Waller parametrization may not be entirely correct, it seems reasonable, within our experimental data, to use it for extrapolating the results of the scattering experiments to 0 K. Equation (13) is used for correcting the results, even though it only considers the z components of $\mathbf{k}$ and $\mathbf{u}_{eff}$, because these should be the dominant terms, particularly at angles near specular.[50]

As mentioned above, only three inelastic features were observed for He scattering from a Xe monolayer. This was strictly true for $\Theta_i = 45°$. Some TOF spectra were taken at $\Theta_i = 60°$. There were two reasons for this. First, we wanted to see if there was any evidence of the longitudinal mode, which should couple better with the incoming beam at more glancing angles. The second reason was to observe the umklapp phonons around the rather large $(\overline{22})$ diffraction peak observed at this incident angle. Some of these results are shown in Fig. 16. When the final scattering angles probed are 11° or 15°, only the same three features as observed at $\Theta_i = 45°$ are seen. However, at $\Theta_f = 13°$, there is very clearly another energy loss feature of 8.17 meV. This is very close to three times the lowest energy mode ($3\times2.79 = 8.37$) and is much higher than that expected from a single phonon creation interaction with the longitudinal mode.[21,22] Since the longitudinal mode strongly disperses across the SBZ, any multiphonon interactions with this mode would not show up as well defined peaks.

Also examined, at $\Theta_i = 60°$, were the final scattering angles of 20°, 21°, and 23°, all on the same Xe monolayer. At $\Theta_f = 23°$, there is the hint of an energy loss feature of about 8.09 meV. At $\Theta_f = 21°$, there is a very pronounced energy gain feature of 14.11 meV. This corresponds to five times the lowest energy ($5\times2.79 = 13.95$). Again, this is a relatively sharp feature, and has an energy much higher than that expected for a single phonon annihilation with the longitudinal mode. Finally, at $\Theta_f = 20°$, there is another rather small energy gain feature of about 8.74 meV. Because of its size and position with respect to the single phonon annihilation peak, there is a large uncertainty in this value, but it appears to be about three times the lowest energy interaction observed.

INELASTIC SCATTERING: PROBABILITIES AND LINEWIDTHS

Having extracted the energies of the inelastic transitions, we decided to look at the spectra in more detail, and try to extract some information on the inelastic scattering probabilities and linewidths. The first task was to characterize the incident He beam. This was assumed to be a shifted Maxwellian, where the number density has the distribution given by Eq. (8). The experimentally measured TOF spectrum is primarily a convolution of the beam's velocity distribution and chopper gating function. This latter function was simulated by overlapping the beam defining aperture with the moving slit of the mechanical chopper. First, the flight time of the ions through the quadrupole, $2.48\sqrt{M}\,\mu$s, was subtracted from the observed flight times. This was determined in two ways. First, it was calculated using the geometry and voltages of the ion optics in front of the quadrupole entrance aperture. Second, the time of flights of completely expanded room temperature beams of He, Ne, Ar, Kr, and

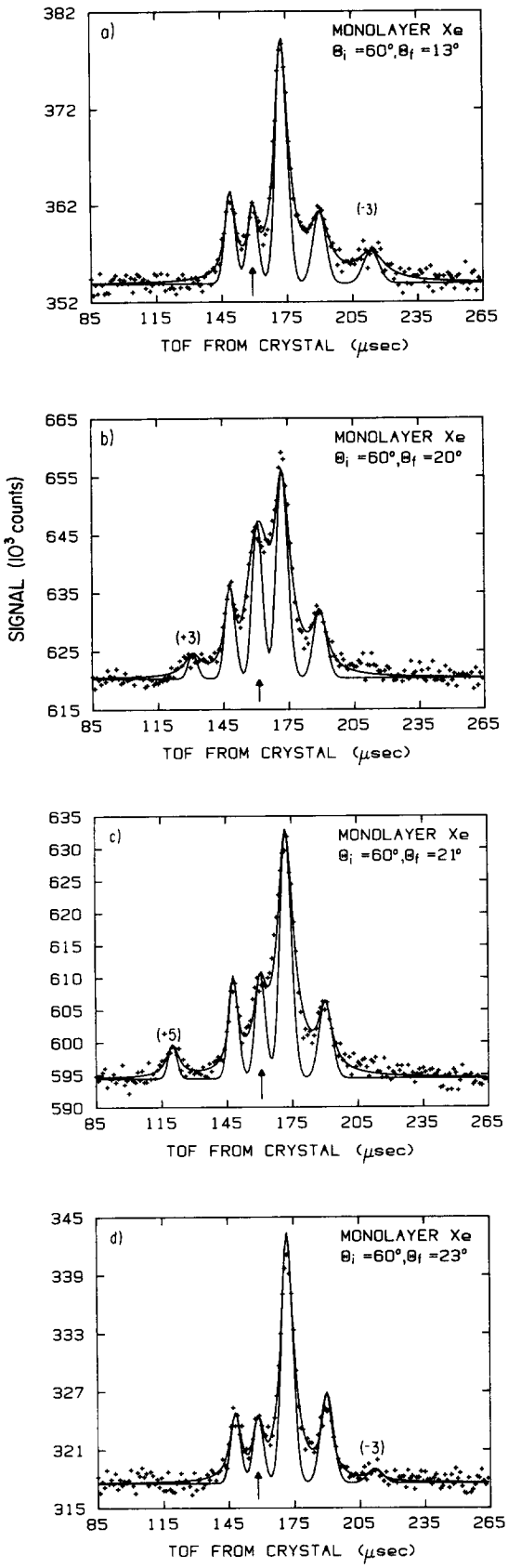

FIG. 16. TOF spectra of an 18 meV He beam scattering from a Xe monolayer physisorbed on Ag(111) along the $\langle 11\bar{2}\rangle$ azimuth, $T_s = 24$ K, $\Theta_i = 60°$, and 1 h of signal averaging. These spectra show unusual features which appear to be due to multiple phonon creation and annihilation. The numbers in parentheses indicate the corresponding number of phonons created or annihilated. For an explanation of the solid lines, see Fig. 6.

Xe ($E = 5/2\, k_b T$) were measured. The latter procedure also indicated that there was a 2 μs offset in the electronics that triggered the MCS. This observation was verified by determining the angular position of diffraction peaks of an H_2 beam scattering from the clean Ag(111) surface.

Once the time of each channel had been determined relative to the chopper position, estimated velocity distribution parameters were convoluted with the shutter function and fit with a nonlinear least-squares routine. The program modified the parameters iteratively until the simulation matched the experimental data. Included in the program was a Gaussian approximation for the ionization probability as a function of distance through the ionizer, since the ionizer length, approximately 2 mm, is a small but significant part of the total flight distance. The result of the data, the simulation, and the difference is shown in Fig. 17.

At this point, we had the width and stream velocity of the incident beam, as well as the experimentally determined energy changes of the inelastically scattered He. These were the inputs to another program that simulated the experimentally observed scattering. In detail, the beam was assumed to have a uniform conical spatial distribution, defined by the nozzle and the 0.020 in. aperture mounted in the source wall between the source and the last region of differential pumping. Using accurate drawings of the machine, the angular divergence of the beam was determined by constructing rays from the nozzle through the series of apertures between the differential pumping stages. By extending the rays to the position of the crystal, the size of the beam at the crystal was determined.

The program digitized the beam distribution, and spatially divided the beam into an x–y grid. The shutter was then moved in discrete time steps across this grid. At each time interval, and for each section of the grid where the beam made it through the chopper, each part of the incident distribution was allowed to interact with phonons determined by the experimental dispersion curves. For each value of energy and parallel momentum exchange, the final scattering angle

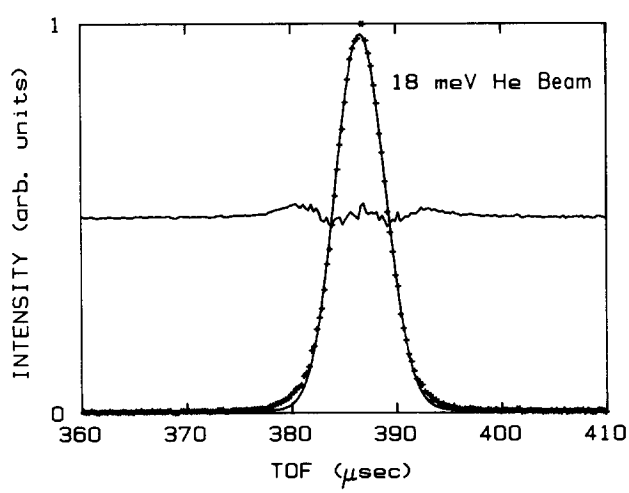

FIG. 17. An example of the TOF spectrum of the incident 18 meV He beam, taken with the detector in the straight-through position. The crosses are the experimental data points, the solid line through the data points is the result of the simulation used to extract the velocity distribution, and the other solid line is the difference, offset half-scale for clarity.

was determined for He atoms in this velocity and position interval. Each section of the beam, after interaction with the crystal, was propagated from the crystal to the detector and, if it was able to pass through the detector apertures, was then added into an array containing intensity as a function of time. The detector could also accept scattered atoms at small out-of-plane angles. Therefore, out-of-plane scattering angles and parallel momenta were allowed, with the energy of interaction determined by the value of **Q** along the $\langle 11\bar{2}\rangle$ azimuth. Basically, the procedure involved integrating the intensity over the observed solid angle. Proper weighting of the intensity for the number density detector was accomplished by conserving the flux of He at the crystal surface. Also, as mentioned above, the flight times were weighted by a Gaussian approximating the ionization probability as a function of distance through the ionizer.

A final weighting was done for the ionization probability as a function of position at the ionizer in a plane perpendicular to the flight path, as the ionizer is not isotropic. To estimate this function, we measured the intensity of a straight through He beam in the scattering plane and perpendicular to it, using a 50 μ detector aperture that could be moved across the face of the ionizer.

To calibrate the simulation, I_{00} was also simulated using the same program. The value for I_{00} was corrected for the experimental broadening of the elastic features that was observed. Inelastic scattering probabilities could then be determined by the ratio of the areas of the peaks in the simulation and the experimental inelastic TOF spectra. The inelastic scattering probability for each peak was determined by taking the ratio of $[(I_{\text{inelastic}}/I_{00})_{\text{exp}}]/[(I_{\text{inelastic}}/I_{00})_{\text{sim}}]$, where the subscripts exp and sim refer to the experimental and simulation results, respectively. This is the number that is reported as probability per steradian normalized by I_{00}, I_{phonon}/I_{00}/sr.

The result of this simulation is shown in Figs. 6, 7, 8, 16, and 30, as the narrower of the solid lines. In these figures, the heights of the peaks have been adjusted to be the same as that of the solid curve that more nearly goes through the data points. This was done to clearly show that the peak widths of the simulations are narrower than the experimental data. It seemed reasonable that the extra width might be due to lifetime broadening.[51] Therefore, a further simulation was done, in which the energies of the transitions, rather than being discrete, were chosen to be Lorentzians centered on the experimental values. For the monolayer, it was simple to get an initial estimate for the width of the Lorentzian, using the difference in the squares of the widths between the fits to the data and the Gaussians of the simpler simulation. Using these initial guesses, the simulation gave the results shown by the solid lines passing throught the data points. The actual line shape of this convolution is not a simple function, and is not symmetric in time space. However, Lorentzians fit the simulations well. Also, since the experimental data were fit to Lorentzians, this seems the most appropriate fitting function. The elastic features in the inelastic scattering spectra were treated as interactions with phonons of zero energy, also broadened in energy. However, in the experimental data, these were sometimes fit with a Gaussian, when a better fit to the entire data was achieved with this fitting function as opposed to a Lorentzian. In this event, the energy broadening function used was a Gaussian, and the elastic feature in the simulation was also fit with a Gaussian.

Since the spectra were signal averaged for about an hour, it was not possible to use a particular monolayer for more than a few runs before it became contaminated. Also, the Ag substrate had to be argon ion sputtered and annealed several times during the course of these experiments. Though the specular He scattering indicated that the surfaces were very similar, they were not exactly the same. To assess the similarity of the monolayers for a particular rare gas, each monolayer grown had at least one TOF spectrum taken at the same angle. The final angle chosen was where the largest inelastic feature had a good signal-to-noise ratio after only 20 min of signal averaging. In many cases, this spectrum was run immediately after the monolayer was grown, and repeated immediately before desorption. If the surface were not allowed to become too contaminated, the results before and after agreed within experimental error. As mentioned in the experimental section, the Xe monolayers showed the widest variation in the specular intensity. The question was whether just normalizing by the specular intensity is sufficient. Figure 18 shows a plot of $I_{\text{inelastic}}/I_0$/sr at

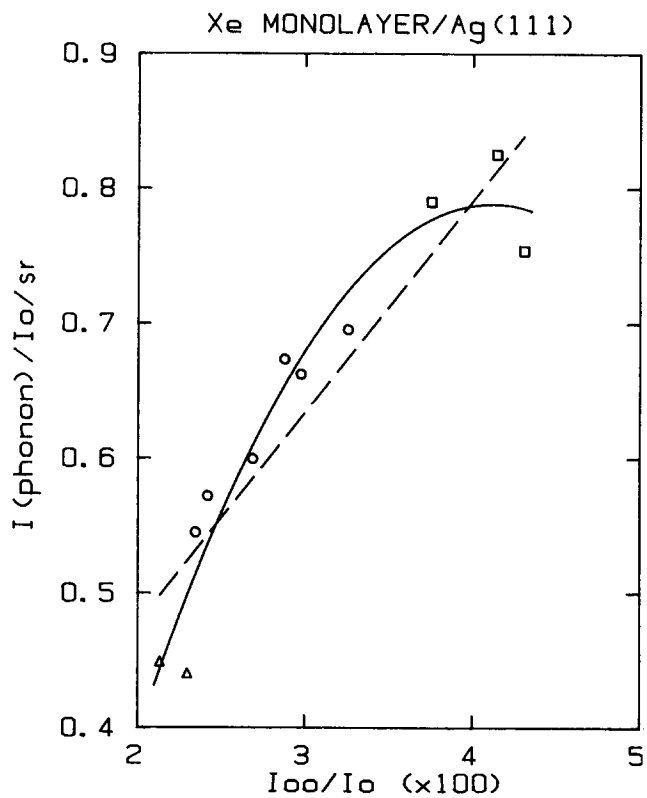

FIG. 18. Plot of the inelastic scattering probabilities (normalized by I_0, the incident beam intensity, rather than I_{00}) vs I_{00}/I_0 for the most intense inelastic transition, involving single phonon creation, of an 18 meV He beam scattering from the Xe monolayers. The results are for the spectra where $\Theta_i = 45°$ and $\Theta_f = 47.9°$. Triangles, circles, and squares represent three different data sets taken at widely separated times. The solid line is a best fit to a quadratic, and the dashed line is the best linear fit. The straight line fit, which does not represent the data quite as well, does not have a slope of 1. This indicates that simply normalizing the inelastic scattering results by I_{00} is not sufficient. An internormalization procedure was therefore devised for the accurate comparison of the relative inelastic scattering probabilities. This is described in the text.

$\Theta_i = 45°$ and $\Theta_f = 47.9°$ (determined by multiplying the inelastic scattering probability by I_{00}/I_0) plotted against I_{00}/I_0 at $\Theta_i = 45°$, for the large phonon creation peak present in the scattering from a Xe monolayer. The curve that best duplicates the data is a quadratic, but even the straight line fit does not have a slope of 1. So, at least for relative comparisons, it seemed best to internormalize the probabilities using the common inelastic spectra rather than the relative reflectivities for different films. This was done by multiplying the inelastic scattering probabilities by the mean of the probability for the most intense inelastic feature of the common spectra divided by the probability of that transition for the particular monolayer. This internormalization was done for each of the rare gases, for all of the features except the one occurring at the position of the elastic channel.

Inelastic scattering probabilities are plotted in Figs. 19–

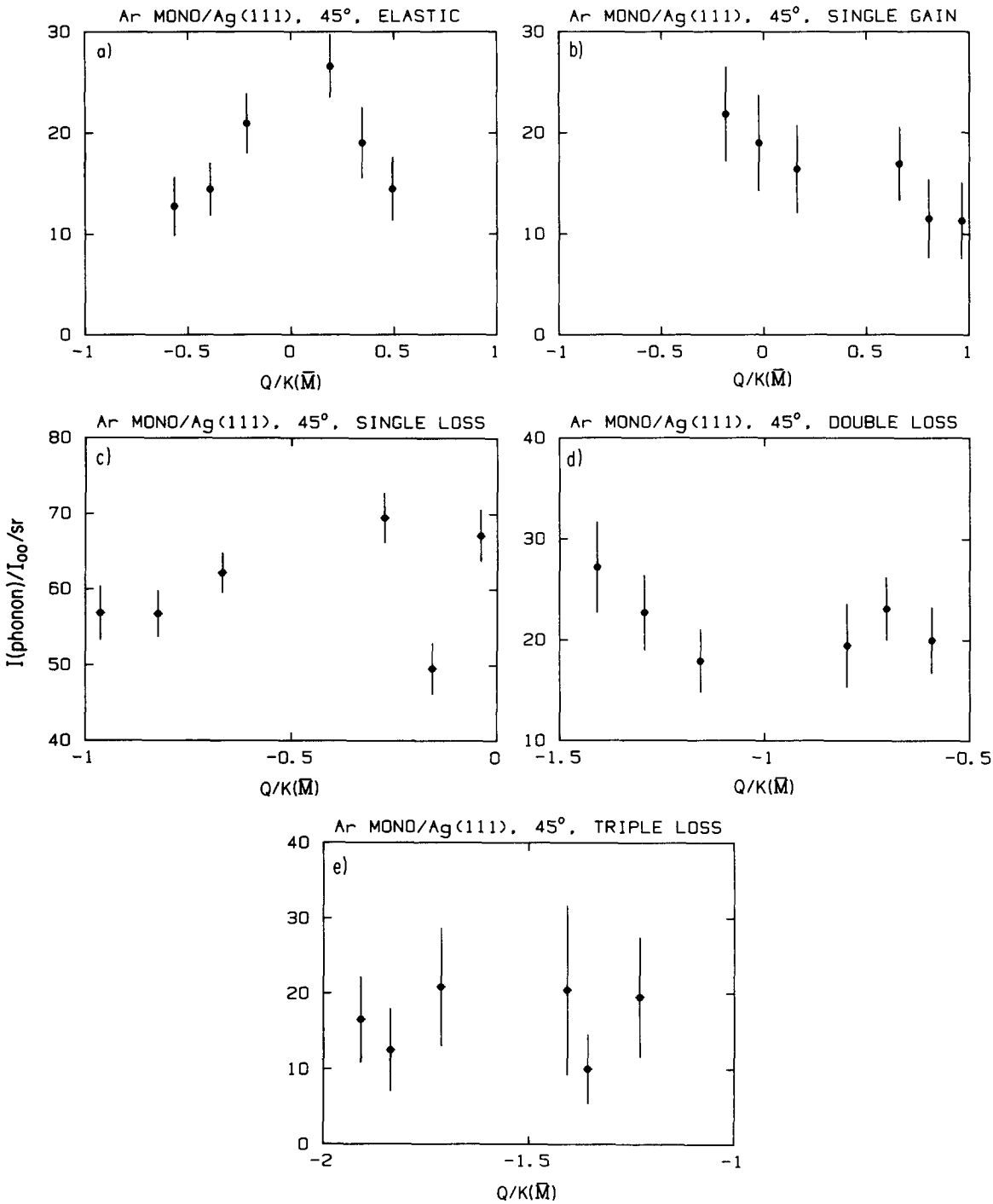

FIG. 19. Inelastic scattering probabilities vs parallel momentum transfer for an 18 meV He beam scattering from the Ar monolayers along the $\langle 11\bar{2}\rangle$ azimuth, with $T_s = 22.5$ K, and $\Theta_i = 45°$. Results are Debye–Waller corrected. The labels loss and gain refer to whether the beam lost or gained energy, respectively. The labels single, double, or triple refer to the amount of energy exchange (see Table II). The results labeled elastic are for the features in the TOF spectra occurring at the position of the elastic channel. These elastic results include the contributions from the specular beam, which become appreciable near the center of the SBZ. $I_{00}/I_0 = 2.10\times 10^{-2}$, which is a Debye–Waller corrected average.

22. For incident angles where few TOF spectra were taken, the results are given in Tables IV–VI. All the results have been normalized to the specular intensity at the incident angle at which the TOF spectra were taken. They have also been Debye–Waller corrected to 0 K, by multiplying $I_{\text{phonon}}/I_{00}/\text{sr}$ by the factor

$$[(\exp(-\Delta k_{\text{zph}}^2\langle u_z^2(0)\rangle))/(\exp(-\Delta k_{\text{zph}}^2\langle u_z^2(T)\rangle))]/[(\exp(-\Delta k_{\text{zsp}}^2\langle u_z^2(0)\rangle))/\exp(-\Delta k_{\text{zsp}}^2\langle u_z^2(T)\rangle))], \quad (16)$$

where the subscripts sp and ph refer to the specular and the inelastic transition, respectively, and $\langle u_z^2(0)\rangle$ and $\langle u_z^2(T)\rangle$ refer to the mean-square displacement of the adsorbed atoms at 0 K and the temperature at which the spectra were taken. Equations (14) and (15) were used to calculate $\langle u_z^2\rangle$ and Δk_z.

For a particular incident angle, there is, in general, no more than a factor of 2 change in the inelastic scattering probabilities across the SBZ associated with the nearest elastic feature. Also, where there is a significant change, *it does not vary monotonically across the SBZ.* This is in contrast with metal surfaces such as Ag(111),[52,53] Ag(001),[36] and Cu(111),[53] as well as the more corrugated Ag(001)-$c(2\times2)$Cl surface,[36] where there is a drastic drop in the inelastic scattering probabilities from zone center to zone edge. In a later section of this paper, we examine the He scattering from clean and partially Xe covered Ag(111) in detail. Though the data are limited, the results for $\Theta_i = 45°$ and 60° presented in Table XI and Fig. 37 clearly show the drastic dropoff in the intensity away from the center of the first SBZ for clean Ag(111).

One of the simpler approaches to calculating single phonon inelastic scattering probabilities involves the distorted wave Born approximation.[54] It has been successfully used for the scattering of He[36,52] and Ne[54] from transition metal surfaces, and can be used to qualitatively examine some of the factors that cause this difference between these surfaces and the rare gas monolayers. The differential cross section per unit surface area for single phonon creation or annihilation is given by

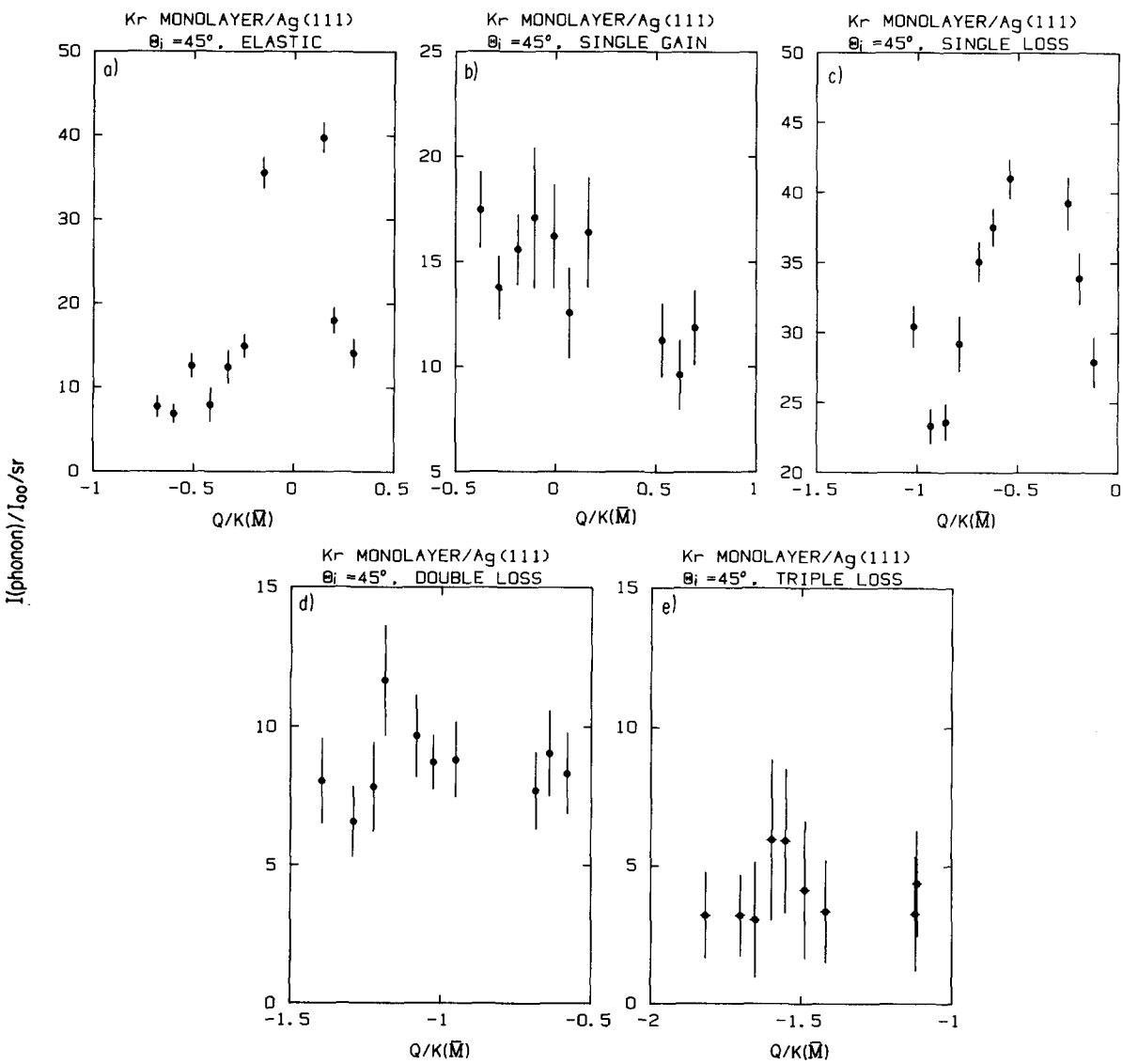

FIG. 20. The same as Fig. 19, but for the Kr monolayers, and $T_s = 24$ K. $I_{00}/I_0 = 3.68\times10^{-2}$, which is a Debye–Waller corrected average.

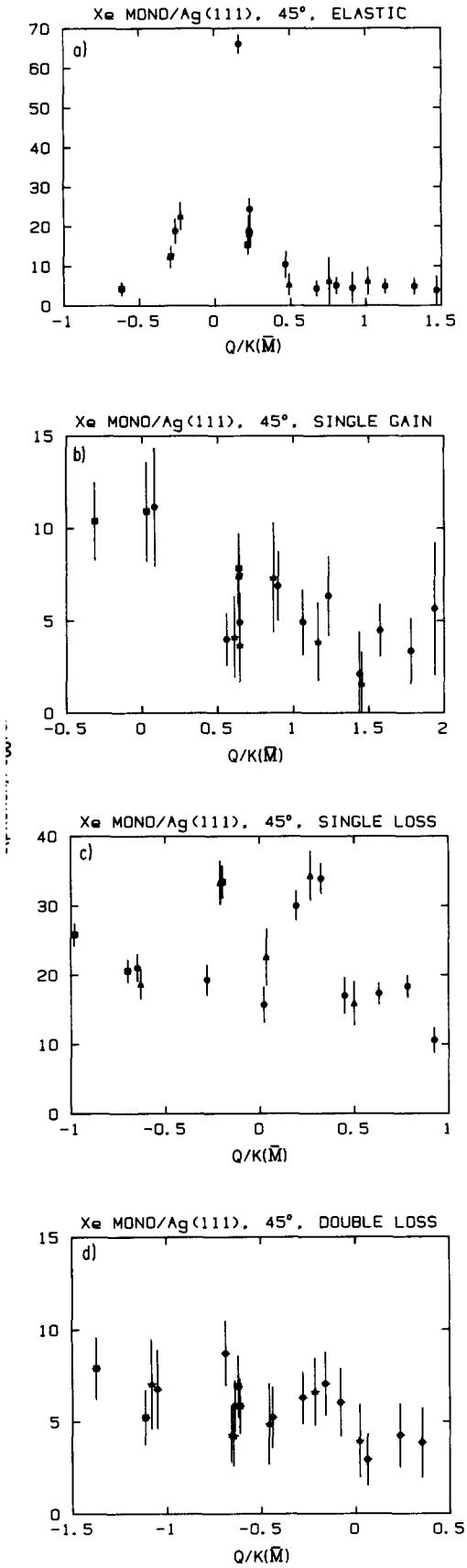

IG. 21. The same as Fig. 19, but for the Xe monolayers, and $T_s = 24$ K. riangles, circles, and squares represent the internormalized results for ıree different data sets collected at widely separated times. $_0/I_0 = 3.30\times10^{-2}$, which is the Debye–Waller corrected probability for ıe monolayer whose internormalization correction was nearly 1.

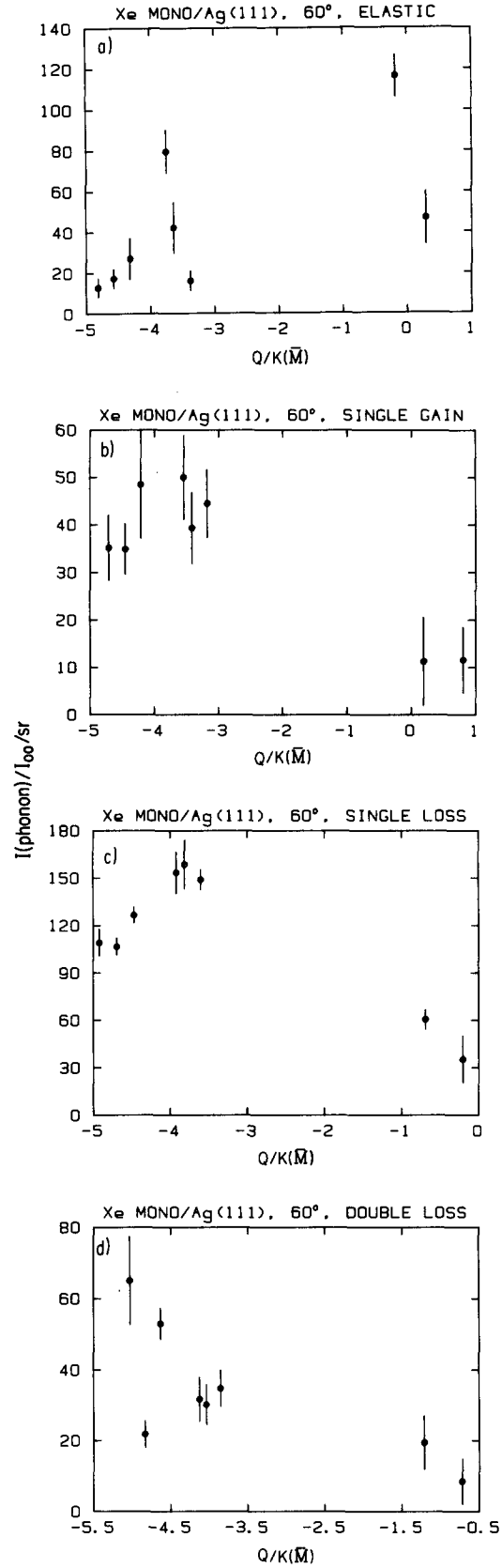

FIG. 22. The same as Fig. 19, but for the Xe monolayers, $T_s = 24$ K, and $\Theta_i = 60°$. Only the two points nearest the center of the first SBZ have been internormalized with the results for $\Theta_i = 45°$. For these, $I_{00}/I_0 = 7.51\times10^{-3}$, which is Debye–Waller corrected. The other points are for two monolayers grown on consecutive days, and have a Debye–Waller corrected average of $I_{00}/I_0 = 1.16\times10^{-2}$. For comparison, $I_{\bar{2}\bar{2}}/I_0 \cong 1\times10^{-2}$, which is also Debye–Waller corrected to 0 K.

TABLE IV. Inelastic scattering probabilities for an 18 meV He beam scattering from the Ar monolayers along the $\langle 11\bar{2}\rangle$ azimuth, with $T_s = 22.5$ K, for two different incident angles. Results have been Debye–Waller corrected to 0 K. Numbers in parentheses are estimated 95% confidence intervals. The labeling of the transitions is the same as in Table II. The Debye–Waller corrected value of $I_{00}/I_0 = 9.29\times10^{-3}$ for $\Theta_i = 60°$, and $I_{00}/I_0 = 2.50\times10^{-2}$ for $\Theta_i = 35°$. Only the results at $\Theta_i = 60°$ have been internormalized with the results at $\Theta_i = 45°$.

	$\Theta_i =$	60°	$\Theta_i =$	35°
Transition	Q/K(M)	Probability	Q/K($\bar{M}$)	Probability
Elastic	0.20(0.02)	34.4(6.3)	0.23(0.02)	22.2(3.7)
+1	0.72(0.02)	13.9(9.4)	0.62(0.02)	13.3(3.8)
−1	−0.34(0.01)	39.8(7.2)	−0.17(0.01)	87.2(3.4)
−2	−1.03(0.01)	28.0(9.5)	−0.60(0.01)	36.5(3.0)
−3	−1.82(0.01)	17(14)	−1.11(0.01)	21.9(6.2)

$$\frac{\partial^2 R}{\partial E_f \partial \Omega_f} = \frac{2}{NM}\sum_{Q,j}\frac{(2ME_f)^{1/2}|k_{zi}||e_z(\mathbf{Q},j)|^2}{\omega_j(\mathbf{Q})}|S|^2 \times\exp(-2W)n[\omega_j(\mathbf{Q})]\exp(-Q^2\bar{z}/\beta) \times\partial(\mathbf{K}_f-\mathbf{K}_i-\mathbf{Q})\partial[E_f-E_i-\omega_j(\mathbf{Q})]. \quad (17)$$

N and M are the dimensions of the Brillouin zone, j refers to the phonon mode, $|e_z(\mathbf{Q},j)|^2$ is the square of the perpendicular displacement of the phonon polarization vector, $\exp(-2W)$ is the Debye–Waller factor, and $n[\omega_j(\mathbf{Q})]$ is the Bose statistical factor. For a hard wall and fast collision times,

$$S = \frac{(p-q)}{\sinh(p-q)}\frac{(p+q)}{\sinh(p+q)} \times\frac{[\sinh(2p)\sinh(2q)]^{1/2}}{(4pq)^{1/2}}, \quad (18)$$

where $p = \pi k_{iz}/\beta$, $q = \pi k_{fz}/\beta$, and β is the curvature of the repulsive wall of the potential, as in Eq. (9). The final term, $\exp(-Q^2\bar{z}/\beta)$, where $\bar{z}$ is the turning point for the scattered He, takes into account the interaction of the He with multiple surface atoms, thus decreasing the probability of observing transitions involving short wavelength phonons.

It is important to note that the cross section is proportional to $n[\omega_j(\mathbf{Q})]/\omega_j(\mathbf{Q})$. For a mode that disperses, going to a higher energy towards the zone edge, this factor is going to cause a falloff in the intensity. For the dispersionless monolayer mode, this factor is a constant. In fact, for the monolayer,

TABLE V. Same as Table IV, for the Kr monolayers at $T_s = 24$ K. $I_{00}/I_0 = 1.46\times10^{-2}$, which has been Debye–Waller corrected to 0 K. The results have not been internormalized with the results at $\Theta_i = 45°$.

	$\Theta_i = 35°$	
Transition	Q/K($\bar{M}$)	Probability
Elastic	−0.28(0.02)	35.6(6.2)
+1	−0.021(0.02)	30(10)
−1	−0.59(0.01)	86.2(5.8)
−2	−0.91(0.01)	43.8(6.4)
−3	···	<8

$$\frac{\partial^2 R}{\partial E_f \partial \Omega_f} \approx C\sum_{Q,j}\exp(-Q^2\bar{z}/\beta)\partial(\mathbf{K}_f-\mathbf{K}_i-\mathbf{Q}) \times\partial[E_f-E_i-\omega_j(Q)] \quad (19)$$

for Θ_f close to Θ_i. The cutoff factor $Q_c = (\beta/\bar{z})^{1/2}$ is still a dominant term in the scattering from transition metal surfaces, particularly for the large interaction radius of Ne.[54] Even without explicitly determining Q_c, this factor is probably larger for the rare gas monolayers because they have a larger lattice constant. This would make the falloff across the zone less steep. Finally, the formula assumes that only the laterally averaged component of the He–surface potential is important. As shown in Fig. 1, higher order Fourier components of the He–rare gas/Ag(111) potential are significant. This further enhances the inelastic scattering probabilities away from the center of the first SBZ for the monolayers. This is certainly a very important factor in the observation of umklapp processes.

The next question to address is the relative probabilities for the scattering. The ratio between transitions involving single phonon annihilation and creation is largely statistical. At the surface temperatures of the experiments, 75% of the oscillators are in the ground state for the Xe and Kr monolayers, and 85% are in the ground state for the Ar monolayer. From this factor alone, one would expect the intensity ratio for the inelastic scattering involving single phonon creation to that involving single phonon annihilation to be about 5:1 for Kr and Xe, and about 6:1 for Ar. In general, data for the Xe monolayer do not show as many phonon creation transitions as for the Ar and Kr monolayer. However, the absolute intensity of the inelastic scattering was the smallest from the Xe monolayer. Therefore, for the Xe spectra, these events may have been lost in the experimental noise.

Some of the probability plots have distinct maxima as a function of momentum transfer. Most noticeable are the single loss for the Kr and Xe monolayers in Figs. 20 and 21. Kinematic focusing (where the scan curve is tangent to the phonon disperion curve) cannot be a contributing factor, as the scan curves are nowhere tangent to the dispersionless Einstein mode. Also, for this dispersionless mode, there are no singularities in the density of states. One possibility for the maxima in the inelastic scattering has to do with the possible contribution from the elastically scattered signal. For example, the region where the single loss probabilities for Kr are peaked are taken at final angles near the specular, where the intensity of the elastic scattering channel becomes quite large. This is shown in Fig. 7, particularly Fig. 7(b). However, the inelastic chanel and the elastic channel are well enough separated that it does not seem likely that the presence of the large elastic feature is greatly perturbing the fits. Also, there is not a peak in the single gain probabilities, which would probably be the case if the increased intensity was a fitting problem. Further, for the Xe monolayer, the probability maxima for parallel momentum loss also occurs near specular angles, but the probability maxima for parallel momentum gain are at final angles well away from the specular angle.

Another possibility for the probability increases exists,

TABLE VI. Same as Table IV, for the Xe monolayers at $T_s = 24$ K. $I_{00}/I_0 = 1.50\times10^{-2}$ for $\Theta_i = 35°$, $I_{00}/I_0 = 6.72\times10^{-2}$ for $\Theta_i = 49.5°$, $I_{00}/I_0 = 1.22\times10^{-2}$ for $\Theta_i = 51.6°$, $I_{00}/I_0 = 5.93\times10^{-3}$ for $\Theta_i = 30°$, and $I_{00}/I_0 = 4.14\times10^{-2}$ for $\Theta_i = 55°$, all of which have been Debye–Waller corrected to 0 K. Only the results at $\Theta_i = 49.5°$ and $\Theta_i = 51.6°$ have not been internormalized with the results at $\Theta_i = 45°$.

	$\Theta_i = 35°$		$\Theta_i = 35°$	
Transition	Q/K(M)	Probability	Q/K(M)	Probability
Elastic	−0.42(0.02)	11.5(4.6)	−0.40(0.02)	15.4(8.2)
+1	−0.16(0.02)	18.6(6.8)	−0.18(0.02)	22(11)
−1	−0.70(0.01)	42.2(4.6)	−0.69(0.01)	42.4(4.4)
−2	−1.02(0.02)	27.4(5.2)	−1.01(0.02)	25.3(4.1)
	$\Theta_i = 49.5°$		$\Theta_i = 51.6°$	
Transition	Q/K(M)	Probability	Q/K(M)	Probability
Elastic	−0.30(0.02)	6.0(1.0)	−0.28(0.02)	24.1(4.9)
+1	0.041(0.020)	10.4(1.9)	0.056(0.020)	25(10)
−1	−0.72(0.01)	29.0(3.3)	−0.73(0.01)	70(14)
−2	−1.17(0.02)	4.3(0.9)	−1.18(0.02)	21.9(5.2)
	$\Theta_i = 30°$		$\Theta_i = 55°$	
Transition	Q/K(M)	Probability	Q/K(M)	Probability
Elastic	0.20(0.02)	82(21)	0.26(0.02)	12.9(2.5)
+1	···	<10	0.72(0.02)	4.0(1.7)
−1	−0.079(0.010)	88(21)	−0.20(0.01)	10.8(2.8)
−2	−0.39(0.02)	42(17)	−0.73(0.02)	3.9(1.8)

which has been theoretically modeled by Hall *et al.*[23] Using a continuum model for the Ag substrate, they suggest that the monolayer Einstein mode couples into the sagittally polarized Ag Rayleigh mode near the position in reciprocal space where they are resonant. This resonance occurs at that point in reciprocal space where the Einstein mode crosses the Ag Rayleigh mode, as depicted in Fig. 23. Since the coupling of these two modes would increase the magnitude of $|e_z(\mathbf{Q},j)|^2$, the intensity of the inelastic scattering should increase. For both the Kr and Xe monolayers, this point is at $Q/K(\bar{M})\approx0.3$. [$K/(\bar{M})$ is the position of the zone edge in reciprocal space, $2\pi/a\sqrt{3}$, where a is the lattice constant.] The position of the maximum for the Kr single creation inelastic scattering probabilities shown in Fig. 20(c) is near this value of parallel momentum transfer. For Xe, Fig. 21(c), the center of the maximum for positive momentum transfer is close to $Q/K(\bar{M})\approx0.3$, but for negative momentum transfer, it is at $Q/K(\bar{M})\approx0.2$. Unfortunately, we have no data points for the Ar monolayer around the position of the crossing. As shown in Fig. 23, there is also a pseudomode for the Ag(111) surface.[55] If the monolayer also coupled to this, the intensity enhancement could be somewhat broader, and centered at a smaller value of $Q/K(\bar{M})$. The exact position of the crossing points may also change depending upon whether the surface force constants for the Ag are changed much by the presence of the adsorbed rare gas.

If this coupling between the adsorbate and substrate increases the inelastic scattering due to phonon creation, it would seem reasonable to also see it for the phonon annihilation transitions. The Kr results do show a slightly greater inelastic scattering probability near the zone center, but it seems to be fairly uniform across the zone center, and the error bars make it difficult to draw any conclusion. The Xe monolayer results also show an enhancement near the center of the first SBZ, but none around the $(\bar{1}\bar{1})$ diffraction peak, which could happen with this mechanism. Again, the error bars are too large to draw any definite conclusion. For the Xe monolayer, transitions due to umklapp phonons at $\Theta_i = 60°$ seem to show an enhancement in the probabilities around

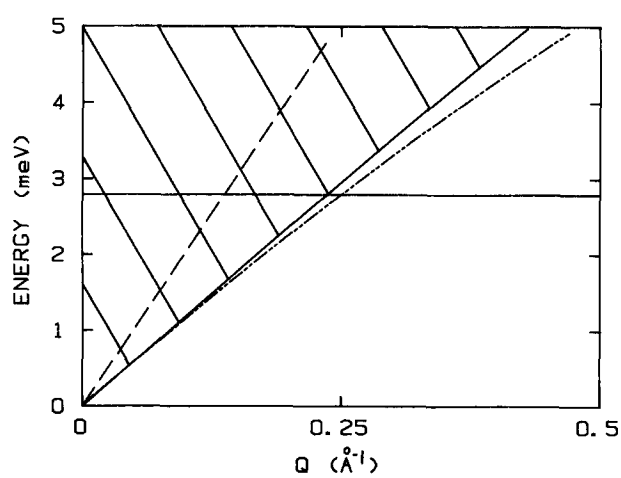

FIG. 23. The dispersion curves for the surface phonons of Ag(111) along the $\langle 11\bar{2}\rangle$ azimuth. The chained line is the position of the Rayleigh wave, the dashed line is the approximate position of the pseudomode, and the shaded area is the surface projection of the bulk modes. The horizonal line is the energy of the $SP_\perp$ mode of the Xe monolayer.

the $(\bar{2}\bar{2})$ diffraction rod for both single phonon creation and annihilation, but they do seem to be peaked at $Q/K(\bar{M}) = 0.2$ on either side of the position of the elastic feature.

We note that such surface resonances induced a hybridization (mixing) of the overlayer Einstein mode and the substrate Rayleigh mode should in fact not only lead to increased $|e_z(\mathbf{Q},j)|^2$, but also induce an energy splitting of the observed inelastic feature. Hall *et al.*[23] have discussed this point in detail, and subsequent measurements by Kern *et al.*[56] for He scattering from Kr/Pt(111) have shown this energy splitting. However, the size of the error bars in the inelastic scattering probability plots point out the difficulty with the experimental apparatus used for these experiments. It would have been desirable to conduct these experiments with better energy and momentum resolution, and a lower He background. It would also help if there were a higher density of experimental points in Figs. 19–21, in order to better resolve subtle probability changes as a function of **Q**.

As shown in Fig. 23, the monolayer phonon energy also overlaps the surface projection of the bulk Ag modes near the zone center. In this region of the SBZ, the monolayer Einstein mode could couple with the surface projection of the Ag bulk modes.[23] In this coupling process, the adatom–

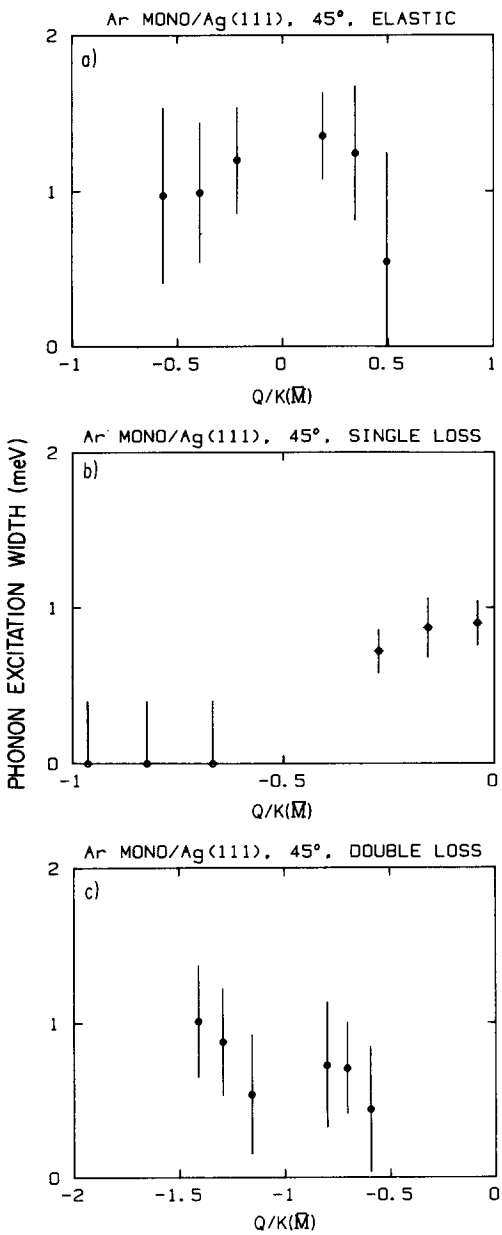

FIG. 24. The FWHM of the energy line shapes used to broaden the inelastic scattering simulations for the Ar monolayers. Data correspond to that used for the inelastic scattering probabilities plotted in Fig. 19. Not plotted because of large error bars, the results for the single gain have an average around 1 meV, and the results for the triple loss have an average around 1.5 meV. The enhanced width seen in the single loss data near the center of the first SBZ is indicative of coupling between the adsorbate Einstein mode and the surface vibrations of the substrate.

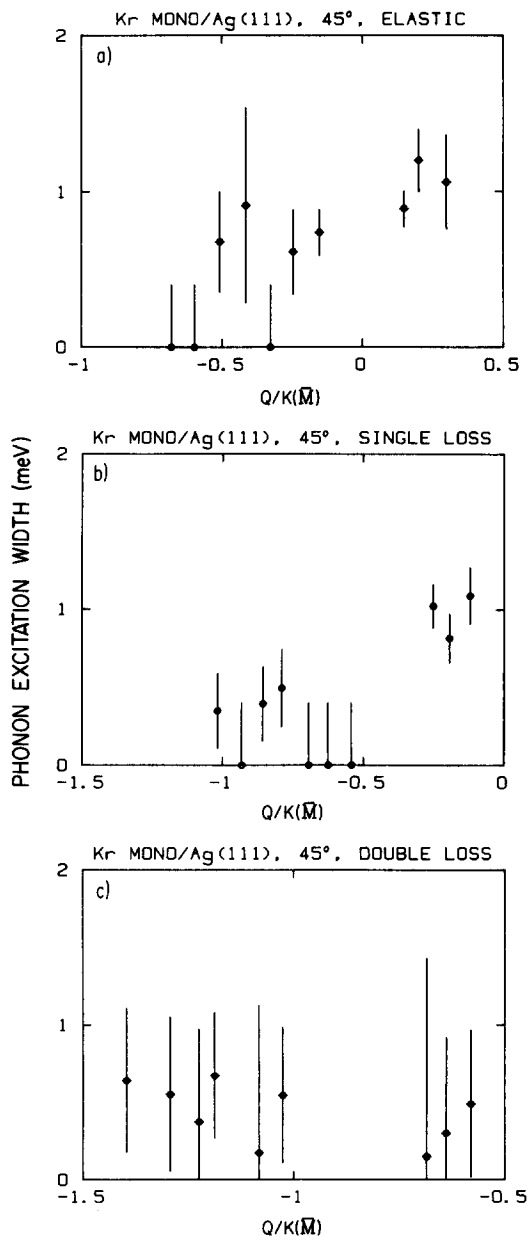

FIG. 25. The FWHM of the energy line shapes used to broaden the inelastic scattering simulations for the Kr monolayers. Data correspond to that used for the inelastic scattering probabilities plotted in Fig. 20. Not plotted because of large error bars, the results for the single gain have an average of about 1 meV, and the results for the triple loss have an average around 1.5 meV. The enhanced width seen in the single loss data near the center of the first SBZ is indicative of coupling between the adsorbate Einstein mode and the surface vibrations of the substrate.

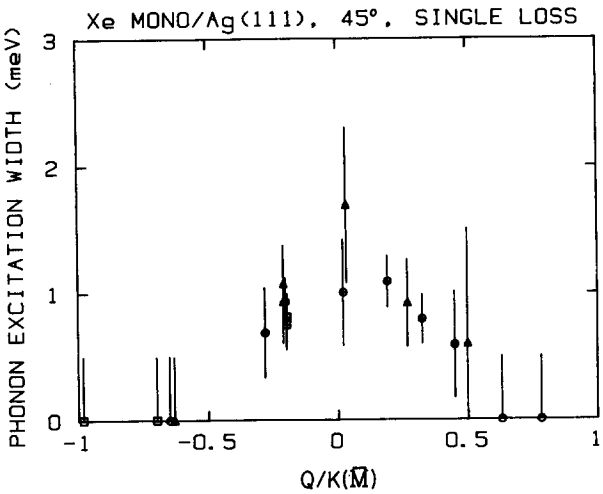

FIG. 26. The FWHM of the energy line shapes used to broaden the inelastic scattering simulations for the Xe monolayer at $\Theta_i = 45°$. Data correspond to that used for the inelastic scattering probabilities plotted in Fig. 21. Only the results for the single loss are plotted, as they have small enough error bars that any width differences as a function of parallel momentum transfer can be observed. For the single gain, the average is < 1 meV, for the double loss, the averge is about 1 meV, and for the elastic, the average is about 1 meV. The enhanced width seen in the single loss data near the center of the first SBZ is indicative of coupling beteen the adsorbate Einstein mode and the surface vibrations of the substrate.

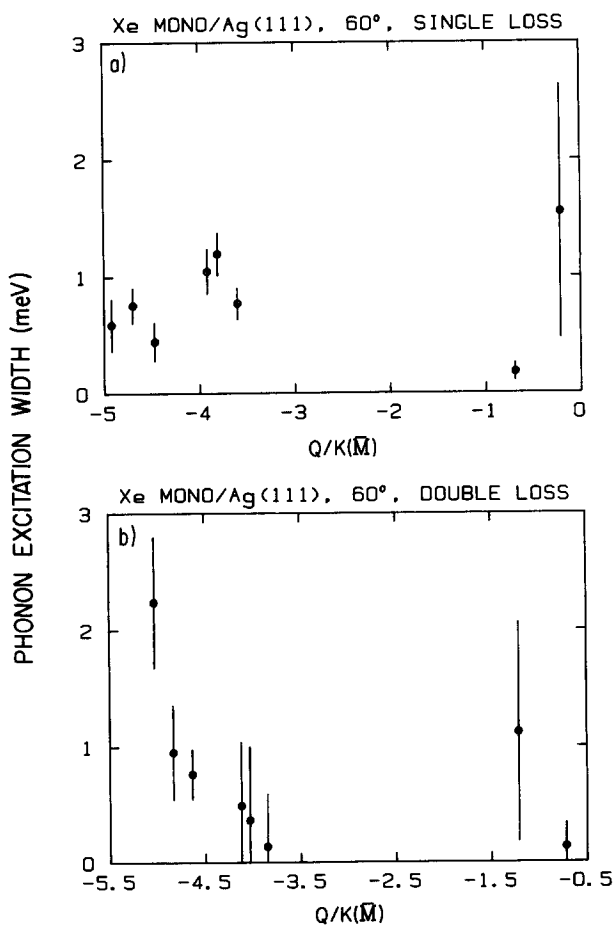

FIG. 27. The FWHM of the energy line shapes used to broaden the inelastic scattering simulations for the Xe monolayer at $\Theta_i = 60°$. Data corresponds to that used for the inelastic scattering probabilities plotted in Fig. 22. For the elastic and single loss, the average value is about 1 meV.

TABLE VII. The FWHM of the energy Lorentzians used to broaden the inelastic scattering simulations for the results in Table IV.

	$\Theta_i = 60°$		$\Theta_i = 35°$	
Transition	Q/K(M)	Width (meV)	Q/K(M)	Width (meV)
Elastic	0.20(0.02)	1.6(0.5)	0.23(0.02)	1.7(0.4)
+1	0.72(0.02)	···	0.62(0.02)	···
−1	−0.34(0.01)	1.1(0.5)	−0.17(0.01)	0.6(0.2)
−2	−1.03(0.01)	1.5(0.8)	−0.60(0.01)	0.3(0.3)
−3	−1.82(0.01)	···	−1.11(0.01)	1.9(0.7)

substrate Einstein vibration is no longer an eigenmode of the system, but can mix with the surface vibrations of the substrate. In the region of this coupling, the Ag(111) surface modes are principally polarized in the plane of the surface, and so would not have much effect on $|e_z(\mathbf{Q},j)|^2$. Since this is the most important component of polarization for determining He scattering intensities, then it would not be expected that these surface resonance modes should affect the inelastic scattering probabilities. However, it seems quite possible that the observed widths of the features in the TOF spectra would be broader near $\bar{\Gamma}$, than near $\bar{M}$. Near $\bar{\Gamma}$, overlap of the surface vibrational density of states of the Ag with the adsorbate Einstein mode will lead to eigenstate mixing, whereas no such overlap exists near $\bar{M}$. One would therefore expect relatively narrow phonon transition widths near the edge of the SBZ, where broadening should be predominately due to anharmonic coupling terms.

Figures 24–27 are plots of the FWHM of the energy Lorentzian used to broaden the simulation, as a function of parallel momentum transfer. Tables VII–X are the values of the widths at incident angles for which not much data were taken. Since the experimental resolution was marginal for the observed broadening, the data have large error bars, and for most cases the results are only good enough to give a bound to its magnitude. However, it appears that for the monolayers of all three rare gases, with the incident He beam at $\Theta_i = 45°$, *the inelastic transition ascribed to single phonon creation is broader near* $\bar{\Gamma}$ *than at* $\bar{M}$. This is especially clear for the Xe monolayer, as seen in Fig. 26, which has the highest density of points taken across the entire first SBZ. Though the exact position in reciprocal space of the drop off of the energy widths is not clear, it definitely happens for $Q/K(\bar{M}) < 0.5$ and so is qualitatively consistent with coupling of the adsorbate Einstein mode with the Ag(111) sur-

TABLE VIII. The FWHM of the energy Lorentzians used to broaden the inelastic scattering simulations for the results in Table V.

	$\Theta_i = 35°$	
Transition	Q/K(M)	Width (meV)
Elastic	−0.28(0.02)	1.1(0.4)
+1	−0.02(0.02)	1.8(1.3)
−1	−0.59(0.01)	0.4(0.3)
−2	−0.91(0.01)	0.9(0.3)

TABLE IX. The FWHM of the energy Lorentzians used to broaden the inelastic scattering simulations for the results in Table VI.

	$\Theta_i = 35°$		$\Theta_i = 35°$	
Transition	Q/K(M)	Width (meV)	Q/K(M)	Width (meV)
Elastic	−0.42(0.02)	<1	−0.40(0.02)	<1
+1	−0.16(0.02)	<3	−0.18(0.02)	2.2(1.4)
−1	−0.70(0.01)	<0.5	−0.69(0.01)	<0.5
−2	−1.02(0.02)	1.0(0.5)	−1.01(0.02)	<1
	$\Theta_i = 49.5°$		$\Theta_i = 51.6°$	
Transition	Q/K(M)	Width (meV)	Q/K(M)	Width (meV)
Elastic	−0.30(0.02)	<1	−0.28(0.02)	0.9(0.6)
+1	0.041(0.020)	1.8(0.7)	0.056(0.020)	···
−1	−0.72(0.01)	<0.5	−0.73(0.01)	<0.5
−2	−1.17(0.02)	<1	−1.18(0.02)	1.2(0.6)
	$\Theta_i = 30°$		$\Theta_i = 55°$	
Transition	Q/K(M)	Width (meV)	Q/K(M)	Width (meV)
Elastic	0.20(0.02)	2.6(0.9)	0.26(0.02)	1.1(0.5)
+1	···	<10	0.72(0.02)	<2
−1	−0.079(0.010)	<2	−0.20(0.01)	1.2(0.6)
−2	−0.39(0.02)	2(1)	−0.73(0.02)	<2

face vibrational modes. Subsequent measurements by Kern *et al.*[56] for He scattering from Kr/Pt(111) also exhibit broadening near $\bar{\Gamma}$. This shows that phonon transition widths can be used to gauge the presence of adsorbate–substrate dynamical coupling, even in the absence of significant enhancement in the inelastic scattering probabilities.

A second observation is that the time-of-flight feature at the elastic channel is in general broader than that of the incident He beam. This would not be the case if it were just due to the incoherent scattering from crystal defects. It seems plausible that there is a contribution due to multiphonon scattering. Since the energies of the Einstein transitions are nearly integral multiples of a single value, the creation and annihilation of the same number of phonons with opposite momenta would result in almost no net energy change. However, each transition does not occur at one discrete energy, and this effect would show up as a net broadening in the "elastic" peak. Contributions from low **Q** vibrations of the Ag(111) substrate may also be present.

There is another mechanism which can influence the inelastic scattering probabilities, the presence of bound states for the He. Their influence on the inelastic scattering from corrugated surfaces has been seen for alkali halides[35,57] and graphite.[58] In the simple free atom approximation, an impinging He atom can be selectively adsorbed on the surface when

$$k_i^2 \pm 2M\omega_j(\mathbf{Q})/h - (\mathbf{K}_i + \mathbf{G} \pm \mathbf{Q})^2 = 2M\epsilon_n/\hbar^2, \tag{20}$$

where M is the mass of the He atom, and ϵ_n is an energy level of the bound state. The magnitude of this effect is shown in Fig. 28 for Ar, Kr, and Xe monolayers. These experiments were done by measuring the specular intensity as a function of Θ_i at 0.2° increments. Boato *et al.*[58] have used this effect to actually map out dispersion curves for corrugated surfaces. It is important to note that our experiments were done at a fixed incident angle. This means that any selective adsorption events due to the incoming beam conditions are most likely to affect all of the observed transitions at that incident angle by an equal amount. The most likely way that these resonances would change the relative probabilities across the SBZ is by a phonon assisted selective adsorption. This could happen when the parallel momentum after an inelastic transition allows the He atom to be selectively adsorbed. Intuitively, it would seem that this mechanism would cause the inelastic scattering probability to decrease at this point. If the He is selectively adsorbed, it is more likely to interact with other phonons, and thus come off with a different **Q** and E_f. However, note that the positions of the enhanced probabilities shown in Fig. 21(c) for Xe are almost symmetrically distributed around the zone center. This would seem to be a most unlikely occurrence if they were due to some sort of selective adsorption effect.

We also decided to examine the effect that incident angle has on phonon transition probabilities. This was done by conducting experiments at different incident angles, and ad-

TABLE X. The parallel momentum transfer, energies, inelastic scattering probabilities, and FWHM of the energy Lorentzians used to broaden the inelastic scattering simulations for the extra features in the Xe TOF spectra taken at $\Theta_i = 60°$ (see the text).

Θ_f	Q/K($\bar{M}$)	Energy (meV)	Probability	Width (meV)
13	−4.99(0.01)	−8.17(0.18)	18.5(5.3)	1.1(0.6)
20	−3.19(0.02)	8.74(0.42)	23(12)	4(3)
21	−2.75(0.03)	14.11(0.56)	27.6(9.1)	3(2)
23	−4.10(0.03)	−8.09(0.24)	5(4)	···

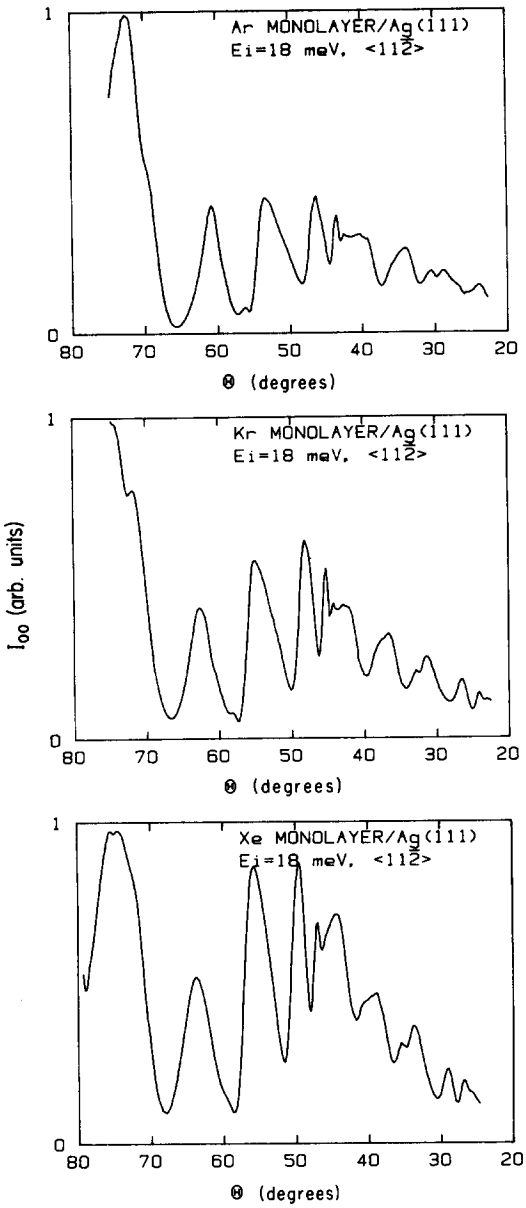

FIG. 28. Experimental results of selective adsorption experiments for Ar, Kr, and Xe monolayers. The conditions are the same as those used to take the TOF spectra. Results are for the specular intensity at 0.2° increments of incident angle.

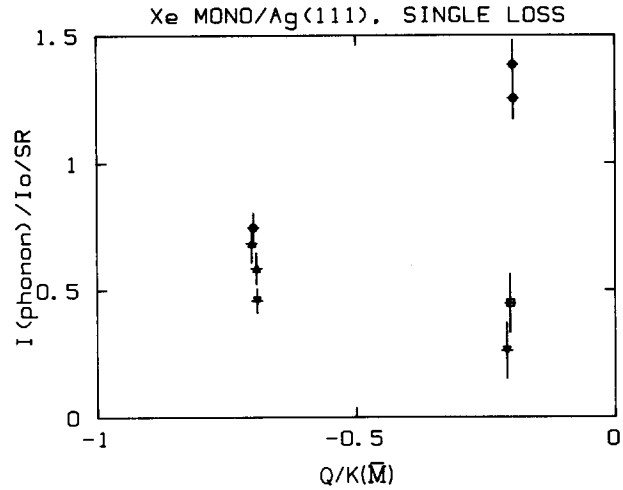

FIG. 29. Inelastic scattering probabilities for 18 meV He scattering from the Xe monolayers along the $\langle 11\bar{2}\rangle$ azimuth at several different incident angles. The results that are plotted are for single phonon creation, multiplied by I_{00}/I_0, so that the results can be directly compared. Plotting symbols represent $\Theta_i = 60°$ (inverted triangles), $\Theta_i = 55°$ (squares), $\Theta_i = 45°$ (circles), and $\Theta_i = 35°$ (triangles).

justing the detector angle so that we could examine transitions with the same **Q**. The results are shown in Fig. 29, for the transition due to single phonon creation at two different values of **Q**. For the purposes of comparison, the results have been multiplied by I_{00}/I_0. The data were taken on two different monolayers, but the duplicate results for $\Theta_i = 45°$ and 35° show that the monolayers were very similar. It is interesting to note that the values are close at $Q/K(\bar{M}) = -0.7$, but only the transition probability at $\Theta_i = 45°$ is enhanced at $Q/K(\bar{M}) = -0.2$. In this case, if the enhancement were due to coupling to the Ag substrate, it would be expected to equally affect all of the results at the same position in the zone, regardless of the incident angle. However, selective adsorption resonances would be dependent on the incident angle. These rather scanty results may argue against the contribution due to coupling. However, the observed broadening is consistent with coupling. The points at $Q/K(\bar{M}) = -0.2$ have widths that are all about 1 meV, while at $Q/K(\bar{M}) = -0.70$, the widths are <0.5 meV.

Results for a similar set of experiments, aimed at examining the affect of elastic scattering resonances on the inelastic scattering probabilities, are shown in Table VI. With the same monolayer, we examined the inelastic scattering probability at $\Theta_i = 49.5°$ and $\Theta_i = 51.6°$. Though only two degrees apart, they correspond to a maximum and minimum, respectively, in the selective adsorption results, Fig. 28. The ratio of the specular scattering intensity is about 5:1, but the intensity of the transition due to single phonon creation is only about 2:1. Therefore, although the intensity of the inelastic scattering increases with the intensity of the associated elastic feature, the scaling is not 1:1. It might be reasonable to think that inelastic scattering should increase when the incident beam is selectively adsorbed, for under these conditions the He atom is spending more time near the surface. If a bound state were near the position of the minima in this case, it might partially explain the scaling.

The widths and inelastic scattering probabilities for the extra feature seen in the TOF spectra taken at $\Theta_i = 60°$ are listed in Table X. At the present time, the origins of these peaks remain a mystery. It is difficult to imagine a process that would involve the annihilation of *five* phonons, and with a fairly large probability! The fact that they come and go over a narrow range of final angles probably argues in favor of some complicated mechanism involving selective adsorption of the incoming He.

Another series of experiments involved investigating the temperature dependence of the inelastic scattering. Figure 30 shows the TOF spectra for a Kr monolayer at three different surface temperatures. The spectra were all taken on the same monolayer, which did not become too badly contaminated over the course of the experiments, as monitored by the intensity of the specular scattering. Also, the experiments were done at the same values of Θ_i and Θ_f, so that the

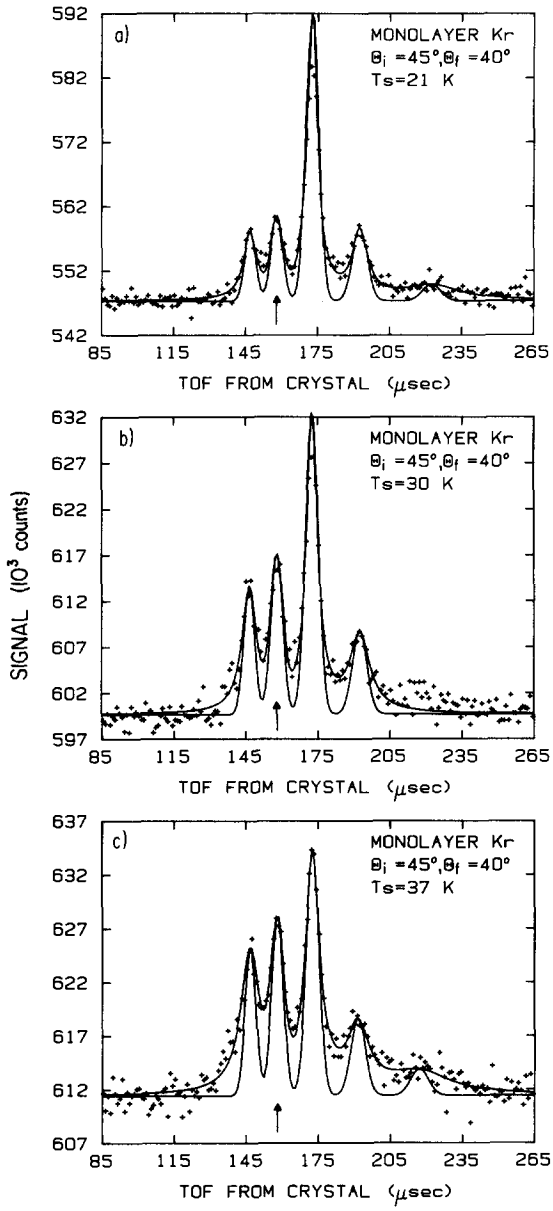

FIG. 30. TOF spectra for an 18 meV He beam scattering from a Kr monolayer along the $\langle 11\bar{2}\rangle$ azimuth, with $\Theta_i = 45°$, $\Theta_f = 40°$, and for three different surface temperatures. The same monolayer was used for all three spectra. The reflectivity of the surface was nearly constant during the course of these experiments, so the surface did not get too badly contaminated. The solid lines are described in the caption of Fig. 6.

results for a particular transition as a function of surface temperature could be directly compared. Similar experiments were done on the Xe monolayer during all three time periods that it was studied. We did not have enough of a temperature range to do temperature dependent scattering from an Ar monolayer.

The first observation is that the energies of the transitons were not temperature dependent, at least within our error bars. This result is not too surprising for an Einstein mode, whose frequency is largely independent of the rare gas–rare gas distances, so that the thermal expansion of the lattice has little effect. Also, the Ag lattice constant does not change much over the temperature ranges used, so the Ag–rare gas holding potential does not change appreciably.

Figures 31 and 32 show the Debye–Waller corrected inelastic scattering probabilities as a function of parallel momentum transfer for Kr and Xe monolayers. For the total probability P_m of the scattering involving an m phonon transition, Meyer developed the following formula[59]:

$$P_m = \exp(-2W_{T_{s=0}})\frac{(2W_{T_{s=T}})^m}{m!}, \tag{21}$$

where $2W$ is the Debye–Waller factor, and the subscripts $T_s = 0$ and $T_s = T$ refer to a surface temperature of 0 K and the surface temperature at which the particular experiment was run. The factor $\exp(-2W_{T_s=0})$ is used instead of $\exp(-2W_{T_s=T})$ given by Meyer, since the results of Figs. 31 and 32 have been Debye–Waller corrected. According to this approximation, all of the inelastic scattering probabilities should increase with increasing temperature, at a rate somewhat larger than a power law dependence of degree m. The results for transitions involving phonon annihilation are expected to increase even faster due to the oscillator statistics. For example, at 21 K, 80% of the oscillators are in the ground state, whereas at 37 K, only 60% are in the ground state. So, neglecting other effects which influence the scattering probabilities, this factor increases the inelastic scattering by a factor of 2 from the lowest to the highest experimental temperatures. It is important to note that the increase in inelastic scattering probabilities shown in Figs. 31 and 32 is a result of the Debye–Waller correction. The observed intensity of the scattering tends to decrease as the temperature is increased, as can be seen in Fig. 30. Only the single gain feature gets larger, and this is due to statistics. The feature at the position of the elastic channel also shows an increase in the inelastic scattering probabilities. This is to be expected if part of the contribution is due to multiphonon scattering.

Figures 33 and 34 are plots of the FWHM of the energy broadening functions used in the scattering simulation for the temperature dependent scattering. The widths near $\bar{M}$, where anharmonic coupling to the Ag(111) surface density of states is the primary source of broadening, should show a greater temperature dependence than the widths at $\bar{\Gamma}$, where harmonic coupling occurs. An increase is observed in the widths for all of the results due to single phonon creation or annihilation for momentum transfers near both $\bar{\Gamma}$ and $\bar{M}$. However, the exact amounts are hard to quantify because of the size of the error bars. Further experiments on this fascinating subject, with an improved instrument, are warranted.

SCATTERING FROM CLEAN AND PARTIALLY Xe COVERED Ag(111) SURFACES

We also looked at the inealstic scattering from partially Xe covered Ag(111). As mentioned in the section on Xe desorption, these involved 6% and 11% to 14% of a monolayer coverage, and for the larger coverages, the adsorbed Xe was probably present as islands. If the inelastic scattering from the Xe were to scale as the relative amount of monolayer coverage, the inelastic scattering from these islands would be very difficult to distinguish above the noise. However, the inelastic scattering of the 18 meV He beam from the Ag(111) surface is clearly seen. A comparison of the TOF spectra for He scattering from a clean Ag(111) surface, and

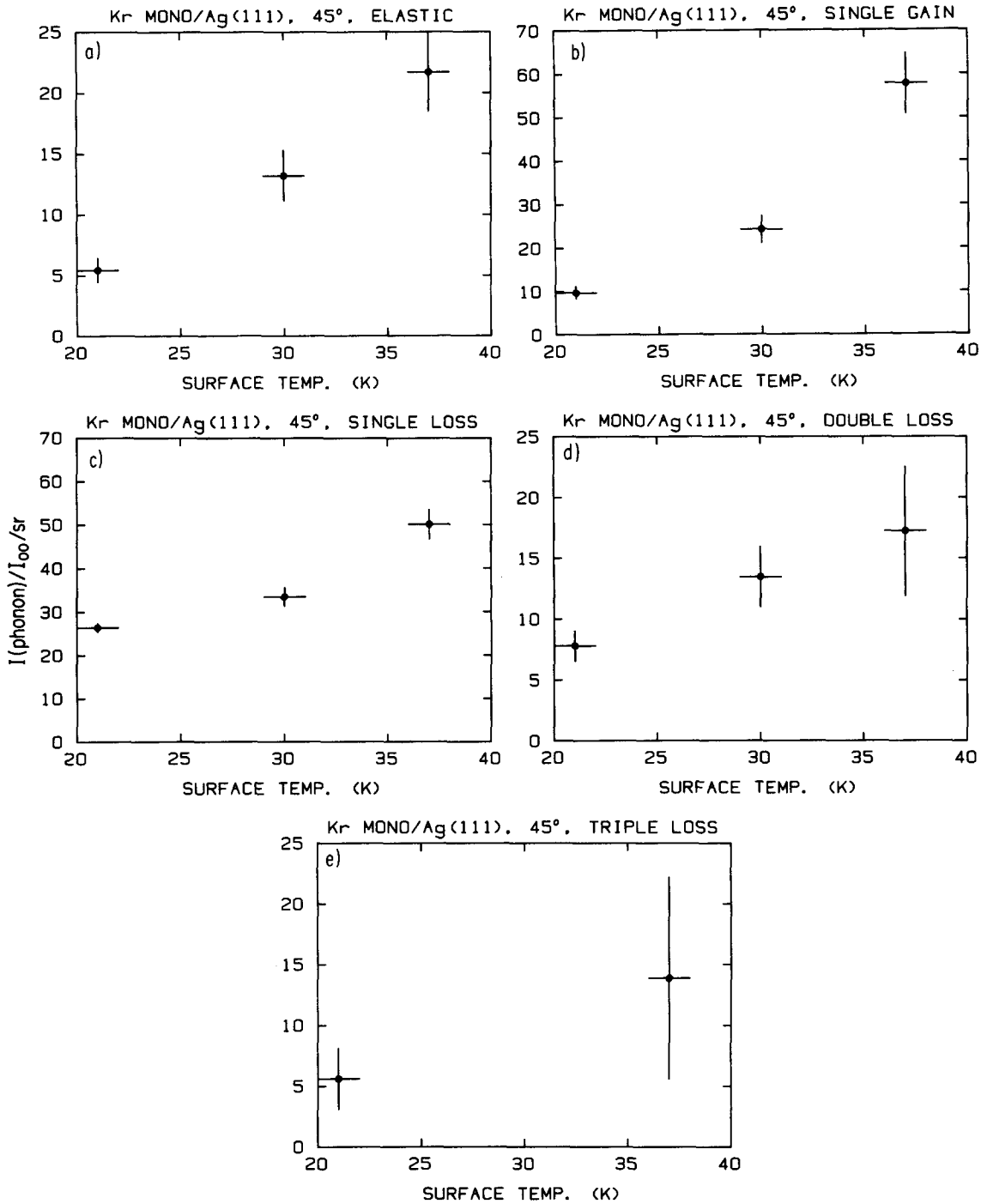

FIG. 31. Inelastic scattering probabilities calculated for the spectra in Fig. 30. The results have been Debye–Waller corrected. $Q/K(\bar{M})$ has the values of -0.42 for the elastic peak, -0.10 for the single gain, -0.78 for the single loss, and -1.17 for the double loss.

a surface with about 13.6% of a monolayer of Xe is shown in Fig. 35. The results for both clean and partial Xe coverage are summarized in Fig. 36. There are some kinematically allowed points near the zone center which are not plotted, but these missing points are largely due to merged peaks in the TOF spectra, rather than the absence of any feature. An example of poorly resolved peaks is shown in Fig. 38, where there are two shoulders on the large peak.

The time-of-flight peaks from which the points in Fig. 36 were determined actually represent a mixture of both scattering from the Rayleigh mode and the pseudomode that has been ascribed to the surface projection of the bulk density of states and a relaxation of the surface force constants.[55] The points for partial Xe coverage are indistinguishable from the points taken from the clean Ag. Since the Xe exists as islands, at least for coverages greater than 11%, this does not show whether or not the presence of the adsorbed Xe modifies the surface force constants of the Ag substrate.

Figure 37 shows the probabilities of the inelastic scattering for both the clean and paritally covered Ag at $\Theta_i = 45°$.

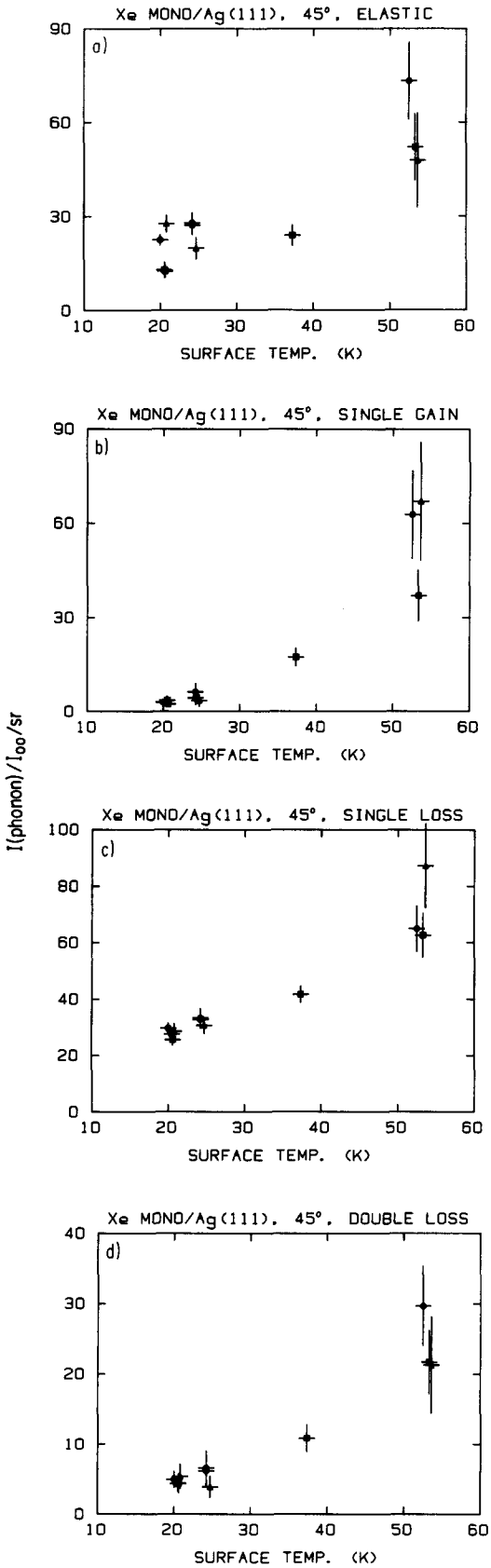

FIG. 32. Inelastic scattering probabilities for an 18 meV He beam scattering from Xe monolayers along the $\langle 11\bar{2}\rangle$ azimuth, with $\Theta_i = 45°$, $\Theta_f = 47.9°$, and for different surface temperatures. Three different monolayers were involved, as indicated by the different plotting symbols. The results have been internormalized at low temperature and Debye–Waller corrected. $Q/K(\bar{M})$ has the values of 0.22 for the elastic peak, 0.64 for the single gain, -0.20 for the single loss, and -0.63 for the double loss.

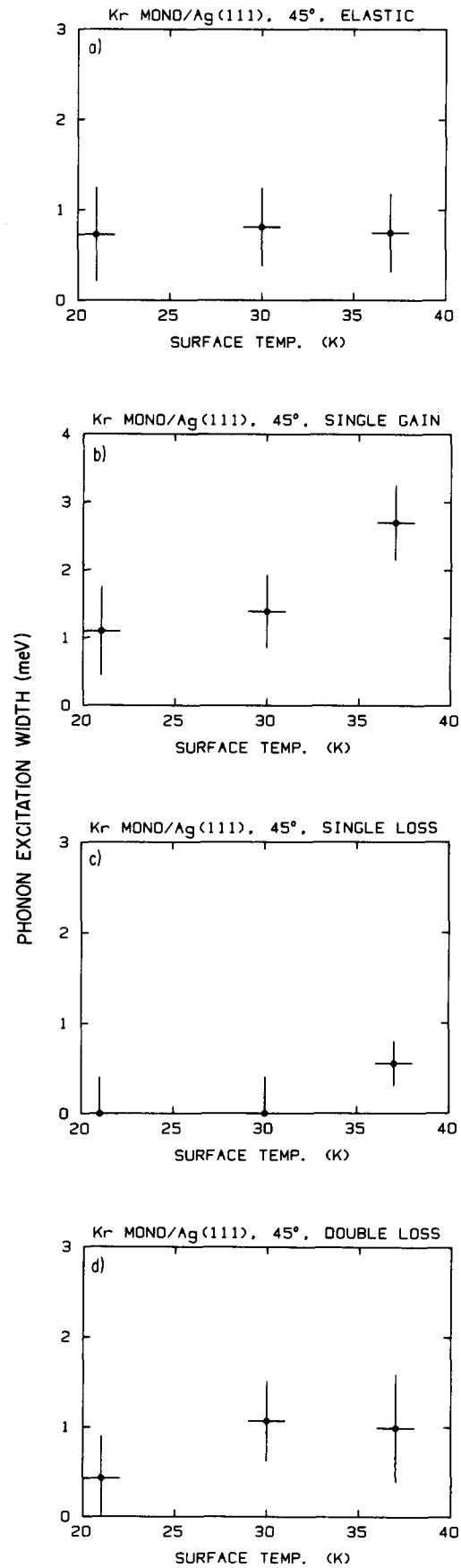

FIG. 33. The FWHM of the energy line shapes used to broaden the inelastic scattering simulations for the TOF spectra in Fig. 30, for the results with sufficiently small error bars.

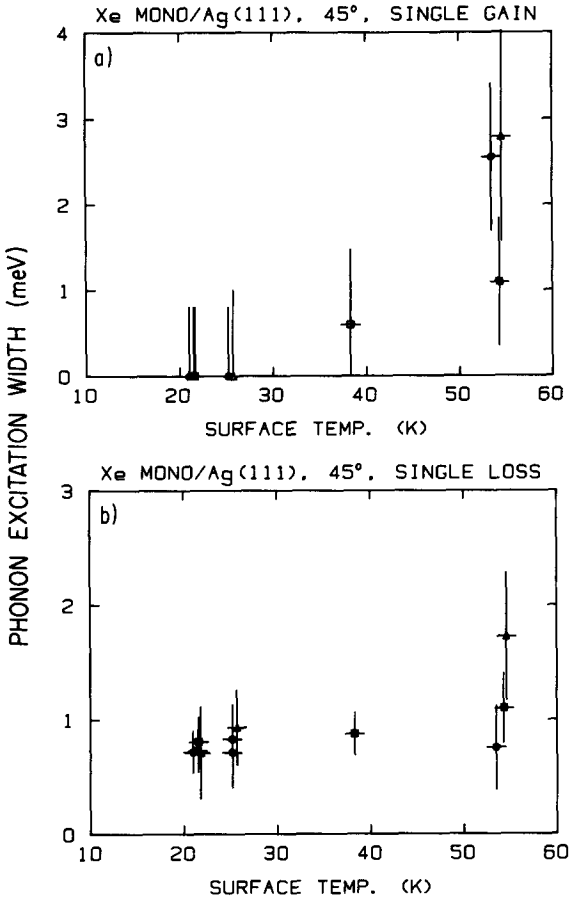

FIG. 34. The FWHM of the energy Lorentzians used to broaden the results of the temperature dependence experiments for the Xe monolayers, for the results with sufficiently small error bars.

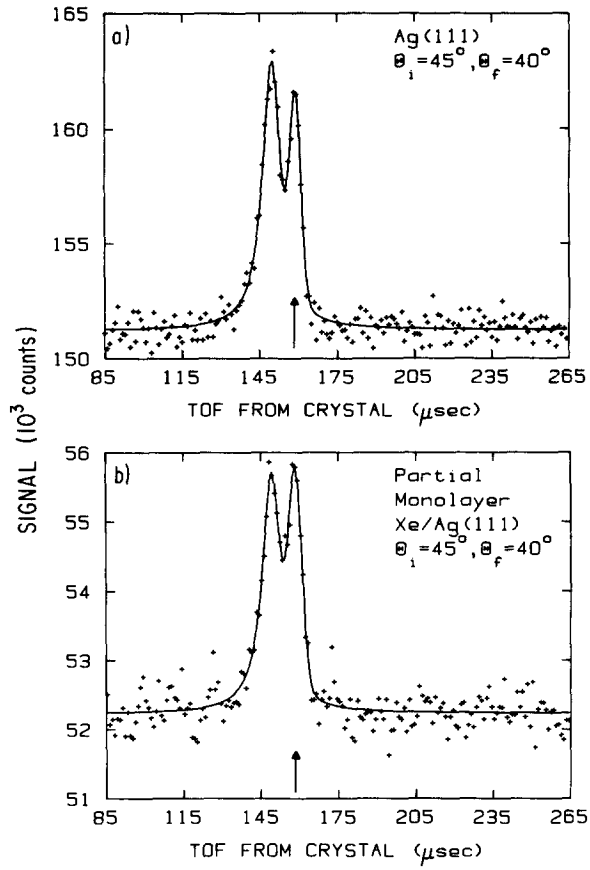

FIG. 35. TOF spectra, taken along the $\langle 11\bar{2}\rangle$ azimuth, of an 18 meV He beam scattering from both a clean Ag(111) surface and the same surface with a coverage of 13.6% of a monolayer Xe. For both spectra, the incident and detector angles were the same, $T_s = 24$ K, and the arrow indicates the position of the elastic channel. The absolute intensities of the two spectra differ because the emission current and signal averaging times were not the same.

Data for the elastic feature and for all of the inelastic features [except the two at $Q/K(\bar{M}) \approx -0.3$, which are clearly not due to the Rayleigh mode] are shown in this figure. When normalized by I_{00}, the probabilities appear to be about the same for both the clean and the partially Xe covered Ag. The rapid monotonic drop in intensity with increasing Q is clearly seen, except for the one anomalous point at $Q/K(\bar{M}) \approx -0.6$. The TOF spectrum for this anomalous point is shown in Fig. 38; the feature is the very broad one seen at long flight times. The explanation for this point is shown in Fig. 39, where scan curves for $\Theta_i = 45°$ are plotted. At $\Theta_f = 48°$, where this spectrum was taken, the scan curve overlaps a large portion of the Rayleigh mode, and so the inelastic feature is due to kinematic focusing. The other two features plotted at $Q/K(\bar{M}) \approx -0.6$ in Fig. 36 were taken at $\Theta_i = 60°$ and $\Theta_f = 70°$, and they also gain intensity from kinematic focusing, though the overlap between the scan curve and the phonon mode is not so great in this case, and the inelastic scattering intensities are weak. The results for the inelastic scattering probabilities at other incident angles are given in Tables XI and XII, for both the clean and partially covered Ag surface.

CONCLUSIONS

This paper is the first in a series that examine our studies of ordered rare gas overlayers physisorbed on Ag(111). In

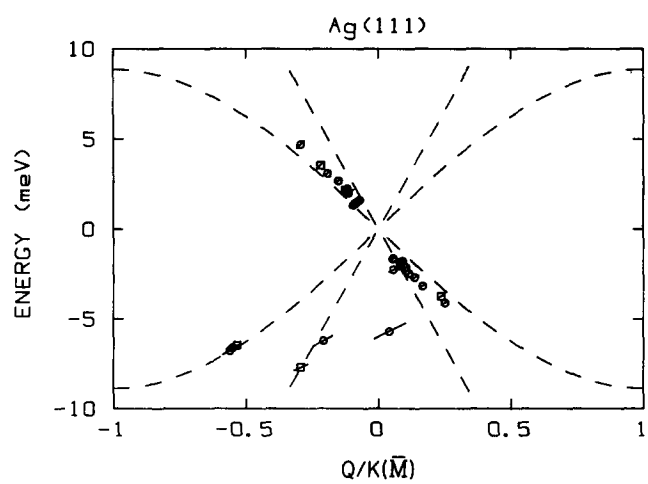

FIG. 36. Energies of the observed inelastic transitions in the $\langle 11\bar{2}\rangle$ azimuth for both clean (boxes) and partially Xe covered (circles) Ag(111). The dashed line at lower energies is the Ag Rayleigh mode, and the other line is approximately the position of the second mode observed by Doak *et al.* (Ref. 37).

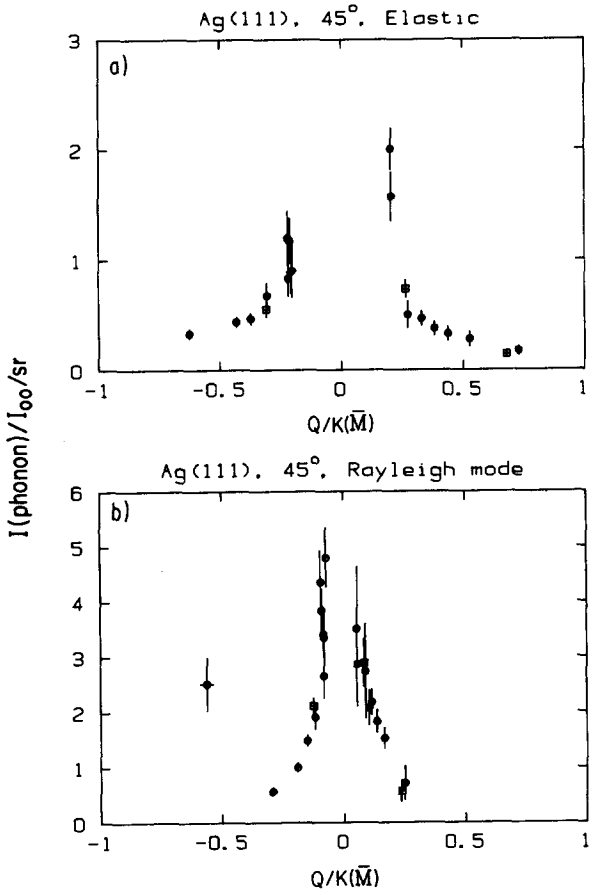

FIG. 37. Plots of the inelastic scattering probabilities of distinct transitions for both clean (boxes) and partially Xe covered (circles) Ag(111). They correspond to the points in Fig. 37 taken at $\Theta_i = 45°$, except for those that cannot be clearly ascribed to the Ag Rayleigh mode. $T_s = 24$ K, and no Debye–Waller correction has been made.

the first part, we examined the desorption kinetics of monolayer Xe using isothermal desorption spectroscopy. For well ordered monolayers, the desorption follows zeroth order kinetics until approximately 90% of the monolayer has desorbed, at which point the desorption kinetics switches to first order. For the zeroth order desorption regime, the activation energy is 4.77 kcal/mol and the preexponential factor is 1.2×10^{28} atoms/(cm^2 s). The first order regime has an activation energy of 4.95 kcal/mol and a preexponential factor of 2×10^{15} s^{-1}. We also *simultaneously* measured nonspecular He diffraction and Xe thermal desorption signals from an isothermally desorbing monolayer at $T_s = 64$ K. These time-resolved diffraction experiments were carried out to see if a correlation existed between the surface structure of adsorbed Xe and its desorption behavior. These measurements revealed that Xe monolayer diffraction persisted until about 90% of the overlayer had desorbed. The presence of the diffraction rods indicates that ordered Xe islands exist throughout the coverage regime exhibiting zeroth order desorption kinetics.

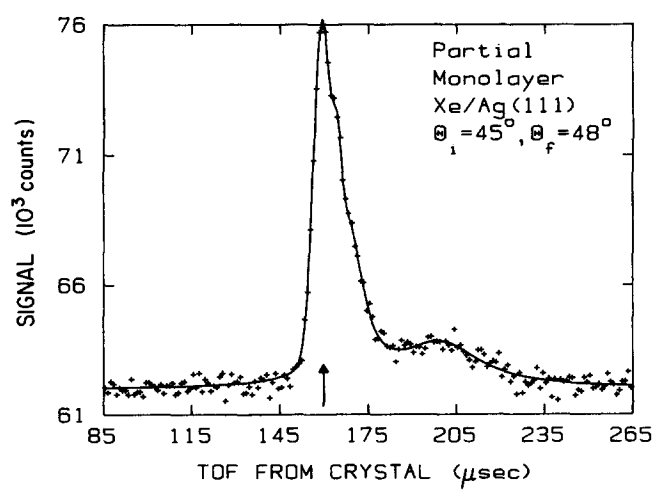

FIG. 38. TOF spectrum of an 18 meV He beam scattering from a Ag(111) surface with a surface coverage of 12.3% of a monolayer of Xe, taken along the $\langle 11\bar{2}\rangle$ azimuth. The arrow indicates the position of the elastic channel. The very broad feature at slow flight times is due to kinematic focusing.

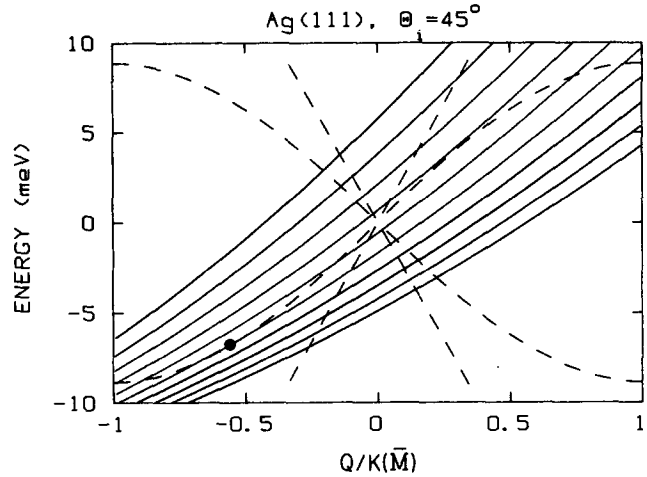

FIG. 39. Scan curves (solid lines) for an 18 meV He beam scattering from a Ag(111) surface along the $\langle 11\bar{2}\rangle$ azimuth. Curves are plotted for $\Theta_i = 45°$, and 2° increments of detector angle, in order top to bottom, from 38° to 56°. Dashed lines are the position of the Ag(111) surface modes observed by Doak *et al.* (Ref. 37). The large dot marks the tangential intersection between the scan curve and the Ag Rayleigh mode at $\Theta_f = 48°$.

In other steady-state experiments, He diffraction from Xe islands was measured for partially covered Ag(111) at $T_s = 25$ K. Here, diffraction from the partial overlayer was measured as a function of sequential pulsed dosing of the substrate. These experiments show that ordered monolayer islands are present for Xe coverages of at least $\geqslant 10\%$. Finally, specular reflection attenuation experiments, which measured the effective scattering cross section per adsorbed Xe atom, were also consistent with the presence of Xe islands for coverages $\geqslant 10\%$.

TABLE XI. Energies, parallel momentum transfer, and inelastic scattering probabilities for the scattering of an 18 meV He beam from Ag(111) along the $\langle 11\bar{2}\rangle$ azimuth. These correspond to inelastic transitions shown in Figs. 12 and 36 which are clearly not associated with the Ag Rayleigh mode. The results have not been Debye–Waller corrected to 0 K.

Θ_i	E(meV)	Q/K(M̄)	Probability
60	−6.47(0.10)	−0.53(0.01)	0.31(0.09)
45	−7.70(0.18)	−0.29(0.02)	0.46(0.13)
35	3.54(0.15)	−0.22(0.01)	1.16(0.06)
60	−2.05(0.10)	0.08(0.01)	1.10(0.45)

TABLE XII. Energies, parallel momentum transfer, and inelastic scattering probabilities for the scattering of an 18 meV He beam from a Ag(111) surface with partial coverages of Xe, taken along with $\langle 11\bar{2}\rangle$ azimuth. These correspond to inelastic transitions shown in Fig. 36 which are clearly not associated with the Ag Rayleigh mode. The results have not been Debye–Waller corrected to 0 K.

Θ_i	E(meV)	Q/K($\bar{M}$)	Probability
60	−6.60(0.15)	−0.52(0.02)	0.22(0.08)
45	−6.22(0.27)	−0.21(0.04)	1.02(0.27)
60	2.01(0.19)	−0.11(0.02)	1.28(0.25)
45	−5.70(0.44)	0.04(0.06)	0.62(0.44)
60	−2.28(0.13)	0.06(0.02)	1.94(0.23)

The second part of the paper deals with the inelastic scattering of an 18 meV He beam from well-ordered, unconstrained monolayers of Ar, Kr, and Xe physisorbed on Ag(111), and from clean and partially Xe covered Ag(111). The measurements on the monolayers examined the surface vibrations as a function of parallel momentum transfer across the entire surface Brillouin zone. For all of the rare gases, we observe a sagittally polarized mode which is dispersionless. This indicates, for this mode, that the adatoms are behaving as independent Einstein oscillators, vibrating in the rare gas–Ag potential well. This is consistent with the idea that the predominant influence of the substrate on the overlayer is to provide a uniform holding potential. The vibrational frequency of the Einstein mode gives the curvature at the minimum of the potential well. Parametrized physisorption potentials for RG–Ag(111), RG = [Ar,Kr,Xe], are constructed using the results. Even within the rigid substrate limit there should be two other modes present for a supported monolayer, one being longitudinally and the other transversely polarized. Kinematically, the longitudinal mode should have been observable. There are predominately two reasons which explain the absence in our data of inelastic scattering from this mode: (i) The cross sections are expected to be low due to the absence of displacements perpendicular to the surface for this mode and (ii) the sensitivity of our measurements was limited by the high mass four background in the detector. Precise estimates of our scattering probability for the longitudinal mode will have to await the outcome of detailed scattering calculations. The guidance obtained from such calculations may be very useful in searching for the signature of this mode. Perhaps using extreme glancing incidence angles or observing high order umklapp processes will be helpful.

We also extracted inelastic scattering probabilities and linewidths as a function of parallel momentum transfer, incident kinematics, and surface temperature. These detailed measurements, taken in conjunction with our elastic scattering results that will be presented in a forthcoming paper, provide a superb data base against which various approximations used in gas–surface scattering calculations can be tested. We wish to emphasize that these rare gas surfaces are nearly ideal model systems for refining theoretical scattering methods, as the He–rare gas, rare gas–rare gas, and He–Ag substrate potentials are all fairly well known. The presence of the Einstein mode, which is polarized normal to the surface and dominates the inelastic scattering, further simplifies theoretical treatment.

The inelastic scattering probabilities that were extracted from these measurements also yielded information about the influence that the dynamical properties of the substrate may exert on the dynamical properties of the overlayers. Near $\bar{\Gamma}$, the frequency of the adsorbate Einstein mode overlaps those of the substrate arising from the surface projection of the substrate's bulk density of vibrational states. Further from the center of the surface Brillouin zone, the frequency of the monolayer Einstein mode crosses that of the Ag Rayleigh mode. Finally, near $\bar{M}$, the frequency of the Einstein mode lies well below the frequencies of any of the substrate modes. We observe that the inelastic scattering probabilities for single phonon creation show an enhancement at the position in reciprocal space where the frequency of the monolayer mode for Kr and Xe crosses the Ag Rayleigh mode. This is one of the characteristics expected for a surface resonance involving hybridization of adsorbate vibrations which have similar **Q**, E, and displacement polarization. An additional result that may occur due to this mixing is a splitting of the Einstein mode into two modes, with different vibrational frequencies, near the overlap region. Such behavior was not observed in these experiments, most probably due to limited **Q** and energy resolution. Quantatative explanation of the observed inelastic scattering variations as a function of **Q** will have to await accurate scattering calculations which explicitly take into account the dynamical properties of both the overlayer and the substrate.

The linewidths of the inelastic scattering transitions also show a dependence on parallel momentum transfer. Clearly, for the inelastic features corresponding to single phonon creation for all three rare gas monolayers, the transition linewidths are larger where the monolayer frequency overlaps those of the Ag substrate, i.e., between $\bar{\Gamma}$ and the adsorbate Einstein mode–Ag Rayleigh mode crossing point. One possible explanation of this is, again, coupling between the adsorbate–surface mode and substrate vibrations present at the Ag surface. Here, line shape broadening arises in the overlap region due to mixing of adsorbate and substrate vibrational wave functions. The lack of overlap near $\bar{M}$ means that the coupling must take place through a more improbable multiphonon transition. Preliminary temperature dependent transition line shape measurements were attempted near $\bar{\Gamma}$ and $\bar{M}$ in order to assess the relative importance of harmonic and anharmonic coupling terms in these two regions. Unfortunately, the results are inconclusive, probably due to the need for higher resolution experiments.

We wish to conclude this paper by emphasizing the point that inelastic He scattering measurements are rapidly developing into a very powerful probe for studying the dynamical properties of surfaces. Single phonon scattering experiments can certainly be used to obtain surface phonon dispersion relations for clean and adsorbate covered surfaces. This information can be used, when combined with lattice dynamics and molecular dynamics calculations, to determine the forces that are present at material interfaces.

In addition, measurements of inelastic scattering transition probabilities and line shapes, taken as a function of fixed wave vector and temperature, hold the promise of revealing how the *dynamical* properties of ordered overlayers and thin films are influenced by the *dynamical* properties of the substrate. Evidence supporting this point was presented in this paper—in spite of the resolution limitations imposed by the apparatus we used. The advent of higher performance scattering instruments will yield a wealth of new information about the structural and dynamical properties of surfaces.

ACKNOWLEDGMENTS

We would like to thank C. F. Yu and D. Padowitz for experimental assistance, and Burl M. Hall, D. L. Mills, and J. E. Black for theoretical collaboration. We also thank M. B. Webb, L. W. Bruch, and M. L. Klein for valuable discussions. This work was supported, in part, by the U.S. Office of Naval Research and the National Science Foundation Materials Research Laboratory at the University of Chicago, DMR-8519460. S. J. S. also acknowledges support from a Camille and Henry Dreyfus Young Faculty Grant, and an I. B. M. Faculty Development Award.

[1]R. J. Birgenau and P. M. Horn, Science **232**, 329 (1986).
[2]*Rare Gas Solids*, edited by M. L. Klein and J. A. Venables (Academic, London, 1977).
[3]P. I. Cohen, J. Unguris, and M. B. Webb, Surf. Sci. **58**, 429 (1976).
[4]L. W. Bruch, P. I. Cohen, and M. B. Webb, Surf. Sci. **59**, 1 (1976).
[5]L. W. Bruch, J. Unguris, and M. B. Webb, Surf. Sci. **87**, 437 (1979).
[6]J. Unguris, L. W. Bruch, E. R. Moog, and M. B. Webb, Surf. Sci. **87**, 415 (1979).
[7]L. W. Bruch and J. M. Phillips, Surf. Sci. **91**, 1 (1980).
[8]J. Unguris, L. W. Bruch, E. R. Moog, and M. B. Webb, Surf. Sci. **109**, 522 (1981).
[9]J. Unguris, L. W. Bruch, M. B. Webb, and J. M. Phillips, Surf. Sci. **114**, 219 (1982).
[10]K. D. Gibson and S. J. Sibener, J. Vac. Sci. Technol. A **3**, 1453 (1985).
[11]K. D. Gibson and S. J. Sibener, Phys. Rev. Lett. **55**, 1514 (1985).
[12]K. D. Gibson and S. J. Sibener, Faraday Discuss. Chem. Soc. **80**, 203 (1985).
[13]H. Taub, K. Carneiro, J. K. Kjems, L. Passel, and J. P. McTague, Phys. Rev. B **16**, 4551 (1977).
[14]B. F. Mason and B. R. Williams, Surf. Sci. **111**, 609 (1981).
[15]B. F. Mason and B. R. Williams, Phys. Rev. Lett. **46**, 1138 (1981).
[16]B. F. Mason and B. R. Williams, Surf. Sci. **139**, 173 (1984).
[17]K. Kern, R. David, R. L. Palmer, and G. Comsa, Phys. Rev. Lett. **56**, 2823 (1986).
[18]B. Feuerbacher, in *Vibrational Spectroscopy of Adsorbates*, edited by R. F. Willis (Springer, Berlin, 1980), p. 91.
[19]J. H. Weare, J. Chem. Phys. **61**, 2900 (1974).
[20]H. Ibach and T. S. Rahman, in *Chemistry and Physics of Solid Surfaces*, edited by R. Vanselow and R. Howe (Springer, Berlin, 1984), p. 455.
[21]K. D. Gibson, S. J. Sibener, B. M. Hall, D. L. Mills, and J. E. Black, J. Chem. Phys. **83**, 4256 (1985).
[22]G. G. Cardini, S. F. O'Shea, M. Marchese, and M. L. Klein, Phys. Rev. B **32**, 4261 (1985); G. Cardini, S. F. O'Shea, and M. L. Klein, Faraday Discuss. Chem. Soc. **80**, 227 (1985).
[23]B. Hall, D. L. Mills, and J. E. Black, Phys. Rev. B **32**, 4932 (1985).
[24]C. A. Becker, Ph.D. thesis, University of Chicago, 1980.
[25]R. Opila and R. Gomer, Surf. Sci. **112**, 1 (1981).
[26]J. M. Ziman, *Principles of the Theory of Solids* (Cambridge University, Cambridge, 1972), p. 56.
[27]P. Korpiun and E. Lüscher, in *Rare Gas Solids*, edited by M. L. Klein and J. A. Venables (Academic, London, 1977), Vol. 2, Chap. 12.
[28]K. D. Gibson, C. Cerjan, J. C. Light, and S. J. Sibener, J. Chem. Phys. **88**, 7911 (1988).
[29]R. J. Behm, C. R. Brundle, and K. Wandelt, J. Chem. Phys. **85**, 1061 (1986).
[30]J. A. Venables and M. Bienfait, Surf. Sci. **61**, 667 (1976).
[31]B. Poelsma, L. K. Verheij, and G. Comsa, Phys. Rev. Lett. **51**, 2410 (1983).
[32]B. Poelsma, R. L. Palmer, and G. Comsa, Surf. Sci. **136**, 1 (1984).
[33]T. H. Ellis, G. Scoles, and U. Valbusa, Chem. Phys. Lett. **94**, 247 (1983).
[34]F. O. Goodman and H. Y. Wachman, *Dynamics of Gas–Surface Scattering* (Academic, New York, 1976).
[35]G. Brusdeylins, R. B. Doak, and J. P. Toennies, Phys. Rev. B **27**, 3662 (1983).
[36]W. R. Lambert, M. J. Cardillo, P. L. Trevor, and R. B. Doak, Surf. Sci. **145**, 519 (1984).
[37]R. B. Doak, U. Harten, and J. P. Toennies, Phys. Rev. Lett. **51**, 578 (1983).
[38]J. M. Horne and D. R. Miller, Phys. Rev. Lett. **41**, 511 (1978).
[39]K. Kern, R. David, and G. Comsa, Surf. Sci. **164**, L831 (1985).
[40]K. D. Gibson and S. J. Sibener, J. Chem. Phys. **88**, 7893 (1988).
[41]L. W. Bruch, Surf. Sci. **125**, 194 (1983).
[42]E. Zaremba and W. Kohn, Phys. Rev. B **13**, 2270 (1976).
[43]P. Nordlander and J. Harris, J. Phys. C **17**, 1141 (1984).
[44]R. N. James, *The Optical Principles of the Diffraction of X rays* (Bell, London, 1967).
[45]R. J. Glauber, Phys. Rev. **98**, 1692 (1955).
[46]A. C. Levi and H. Suhl, Surf. Sci. **88**, 221 (1978).
[47]G. Armand, J. Lapujoulade, and Y. Lejay, Surf. Sci. **63**, 143 (1977).
[48]J. L. Beeby, J. Phys. C **4**, L359 (1971).
[49]S. Chung, N. Holter, and M. W. Cole, Phys. Rev. B **31**, 6660 (1985); Surf. Sci. **165**, 466 (1986).
[50]J. Lapujoulade, J. Perreau, and A. Kara, Surf. Sci. **129**, 59 (1983).
[51]B. N. Brockhouse in *Phonons and Phonon Interactions*, edited by T. A. Bak (Benjamin, Reading, 1964), p. 221.
[52]V. Celli, G. Benedek, U. Harten, J. P. Toennies, R. B. Doak, and V. Bortolani, Surf. Sci. **143**, L376 (1984).
[53]D. Eichenauer, U. Harten, J. P. Toennies, and V. Celli, J. Chem. Phys. **86**, 3693 (1987).
[54]V. Bortolani, A. Franchini, F. Nizzoli, G. Santoro, G. Benedek, and V. Celli, Surf. Sci. **128**, 249 (1983).
[55]V. Bortolani, A. Franchini, F. Nizzoli, and G. Santoro, Phys. Rev. Lett. **52**, 429 (1984).
[56]K. Kern, P. Zeppenfeld, R. David, and G. Comsa, Phys. Rev. B **35**, 886 (1987).
[57]G. Lilienkamp and J. P. Toennies, J. Chem. Phys. **78**, 5210 (1983).
[58]G. Boato, P. Cantini, C. Salvo, R. Tatarek, and S. Terrini, Surf. Sci. **114**, 485 (1982).
[59]H.-D. Meyer, Surf. Sci. **104**, 117 (1981).